



Journal of Geophysical Research: Oceans

RESEARCH ARTICLE

10.1029/2018JC014438

Key Points:

- The respective signature of balanced motions and internal gravity waves on different surface oceanic fields has been revealed
- The World Ocean reveal a complex picture worldwide of the partition of motions between balanced motions and internal gravity waves
- The synergy of using present and future satellite observations can be exploited to assess the oceanic kinetic energy on a global scale

Correspondence to:

H. S. Torres,
hector.torres.gutierrez@jpl.nasa.gov

Citation:

Torres, H. S., Klein, P., Menemenlis, D., Qiu, B., Su, Z., Wang, J., et al. (2018). Partitioning ocean motions into balanced motions and internal gravity waves: A modeling study in anticipation of future space missions. *Journal of Geophysical Research: Oceans*, 123. <https://doi.org/10.1029/2018JC014438>

Received 2 AUG 2018

Accepted 22 OCT 2018

Accepted article online 26 OCT 2018

Partitioning Ocean Motions Into Balanced Motions and Internal Gravity Waves: A Modeling Study in Anticipation of Future Space Missions

Hector S. Torres¹ , Patrice Klein^{1,2} , Dimitris Menemenlis¹, Bo Qiu³ , Zhan Su¹ , Jinbo Wang¹ , Shuiming Chen³ , and Lee-Lueng Fu¹

¹Jet Propulsion Laboratory/California Institute of Technology, Pasadena, CA, USA, ²Lops Ifremer/CNRS, Plouzané, France,

³Department of Oceanography, University of Hawaii at Manoa, Honolulu, HI, USA

Abstract Internal gravity waves (IGWs) and balanced motions (BMs) with scales <100-km capture most of the vertical velocity field in the upper ocean. They have, however, different impacts on the ocean energy budget, which explains the need to partition motions into BMs and IGWs. One way is to exploit the synergy of using different satellite observations, the only observations with global coverage, and a reasonable spatial and temporal resolution. But we need first to characterize and understand their signatures on the different surface oceanic fields. This study addresses this issue by using an ocean global numerical simulation with high-resolution (1/48°). Our methodology is based on the analysis of the 12,000 frequency-wave number spectra to discriminate these two classes of motions in the surface kinetic energy, sea surface height, sea surface temperature, sea surface salinity, relative vorticity, and divergence fields and for two seasons. Results reveal a complex picture worldwide of the partition of motions between IGWs and BMs in the different surface fields, depending on the season, the hemisphere, and low and high eddy kinetic energy regions. But they also highlight some generic properties on the impact of these two classes of motions on the different fields. This points to the synergy of using present and future satellite observations to assess the ocean kinetic energy on a global scale. The 12,000 frequency-wave number spectra represent a World Ocean Atlas of the surface ocean dynamics not fully exploited in the present study. We hope the use of this World Ocean Atlas by other studies will lead to extend much these results.

Plain Language Summary Motivation of partitioning surface oceanic motions with scales <100 km into two classes, balanced motions (BMs) and internal gravity waves (IGWs), is that they are known to have different impacts on the ocean kinetic budget although they share the same range of spatial and temporal scales. Satellite observations are the only ones with a global coverage to capture oceanic surface motions. Our motivation of exploiting the synergy of using all these observations is that these two classes of motions can have different signatures on each of these observations. The results reveal a complex picture worldwide of the partition of motions between IGWs and BMs in the different surface fields, depending on the season, the hemisphere, and low and high eddy kinetic energy regions. But they also highlight some generic properties on the impact of these two classes of motions on the different fields. This emphasizes the strong synergy of using present and future satellite observations to diagnose this partition on a global scale. The results can be of interest for Earth Science community because of their consequences on the ocean kinetic energy budget, the physical-biological interactions, and the air-sea interactions.

1. Introduction

Two major classes of motions characterize the ocean kinetic energy (KE): internal gravity waves (IGWs) and balanced motions (BMs). IGWs include waves (such as wind-driven near-inertial motions) with frequencies equal or larger than the Coriolis frequency, f , and spatial scales from hundreds of kilometers to tens of meters. They are characterized by fast propagation ($c = \omega/k > U$, with c the phase speed, ω the frequency, k the wave number, and U the velocity scale) and are often thought to be driven by weakly nonlinear interactions (Alford et al., 2016). IGWs also include internal tides with diurnal and semidiurnal frequencies. BMs are motions in geostrophic or gradient-wind balance, with usually frequencies smaller than f , which do not propagate as fast as IGWs. They are driven by highly nonlinear interactions and involve large-scale motions (>300 km), as well as mesoscale motions (or MBMs) related to eddies with horizontal scales between 50 and 300 km (McWilliams, 2016). They also include smaller scale structures (50 down to 1 km), such as elongated frontal

and small-scale eddy motions also called submesoscale motions (SBMs) in the present study. Although MBMs can be distinguished from IGWs because of their frequency smaller than f , SBMs cannot since they may have frequencies close to or larger than f (i.e., a Rossby number of $O(1)$) and spatial scales similar to IGWs (Alford et al., 2016; Kim et al., 2011; McWilliams, 2016; Savage, Arbic, Richman, et al., 2017). As detailed later, only moving to the spectral space in the frequency-wave number domain should allow to discriminate SBMs from IGWs, which is accessible from numerical simulations with resolution high enough, but not from existing in situ and satellite observations in the open ocean.

Many studies in the last decades have been dedicated to the KE in the world ocean. It is accepted that most of this KE is captured by mesoscale eddies with wavelengths between 100 and 300 km (Ferrari & Wunsch, 2009). These motions are well monitored by conventional altimetry (Chelton et al., 2011). Other energetic motions with these length scales or smaller scales are associated with coherent internal tides and near-inertial motions. KE of coherent internal tides is usually equal or smaller than the eddy kinetic energy depending on the regions (Savage, Arbic, Richman, et al., 2017). They can be easily diagnosed from satellite altimetry observations (Zaron, 2015). Near-inertial motions have KE that is usually less than 10% of the eddy kinetic energy (EKE). Global data sets of surface drifters are now able to monitor this energy reservoir (Lumpkin et al., 2012).

Our study focuses on a class of smaller spatial scales, equal or smaller than 100 km. The need to discriminate BMs and IGWs in these scale ranges, or to partition motions into BM and IGW contributions, comes from the new vision of the SBM impacts on the global ocean dynamics. On one hand, recent studies indicate SBMs capture most of the vertical velocity field associated with balanced motions in the first 500 m below the surface (Klein & Lapeyre, 2009; McWilliams, 2016; Rosso et al., 2014) and consequently have a significant impact on the ocean energy and carbon export budgets. Su et al. (2018) clearly emphasize the specific SBM impacts compared to the MBM impacts: SBMs drive significant upgradient (and not downgradient) vertical heat fluxes (up to 200 W/m^2 when averaged over three months and boxes with $\sim 3^\circ$ in latitude size), whereas MBMs only trigger positive or negative vertical heat fluxes with magnitudes at least three to four times smaller. Other studies further suggest SBMs represent a significant KE source (and not a sink) for larger scales through an inverse KE cascade (Capet et al., 2016; Qiu et al., 2014; Sasaki et al., 2014). On the other hand, IGWs are known to drive a large part of the ocean mixing through their scattering and associated KE cascade toward smaller scales (Polzin & Lvov, 2011). As a consequence, they trigger downgradient vertical fluxes and represent a KE sink for larger scales. This emphasizes the different impacts of SBMs and IGWs in terms of KE budget. Further results from Callies et al. (2015), Rocha, Chereskin, et al. (2016), Rocha, Gille, et al. (2016), and Qiu et al. (2017) indicate IGWs and SBMs are both characterized by a strong seasonality. On one hand, SBMs are much more energetic than IGWs in winter, when surface frontal instabilities at small-scale (such as mixed-layer instabilities) are more efficient because of the large mixed-layer depths (Callies et al., 2015; Mensa et al., 2013; Qiu et al., 2014; Rocha, Gille, et al., 2016; Sasaki et al., 2014; Su et al., 2018). On the other hand, IGWs near the surface are more energetic than SBMs in summer because of the intensification of the higher vertical normal modes due to shallower mixed layers (Callies et al., 2015; Rocha, Gille, et al., 2016).

Since IGWs and SBMs have different impacts on the ocean energy budget but can share the same spatial and temporal scale ranges, an important question is how to discriminate these two classes of motions from observations. One way to answer this question is to exploit the synergy of using different observations. Such direction is motivated by some preliminary results (Rocha, Chereskin, et al., 2016) indicating, for example, that IGWs and SBMs exhibit distinct signatures in the sea surface height (SSH) wave number spectrum and not in the KE spectrum. Consequently, to assess the potential of this synergy, our study aims to analyze the respective impacts of BMs and IGWs on different surface fields, using a novel global numerical simulation (with tides included) performed at high resolution ($1/48^\circ$ in the horizontal, with 90 vertical levels) (Figure 1). The six fields considered include surface ocean currents themselves (or surface KE), and in particular their rotational (relative vorticity or RV) and divergent (DIV) parts, the SSH, and the sea surface temperature (SST) and sea surface salinity (SSS). One reason to focus on these fields is that existing and future satellite observations are the only ones allowing to get information on these fields with a global coverage and reasonable spatial and temporal resolutions, although each of these satellite datasets has its own limitations. These observations include existing high-resolution satellite images (as SST images) and also those from the new altimeter mission (SWOT, for surface water and ocean topography) scheduled to be launched in 2021. SWOT should allow to diagnose SSH with a resolution of $O(10 \text{ km})$ (Fu & Ferrari, 2008), that is, 10 times

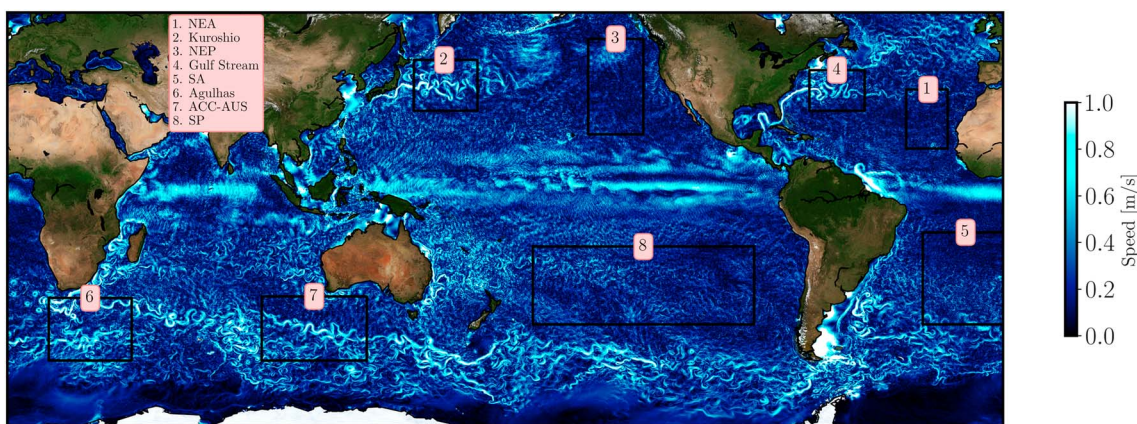


Figure 1. Snapshot of the global surface speed from the LLC4320 simulation. The square boxes highlight the regions with high- and low-kinetic energy discussed in the section 4.

higher than conventional altimeters. Future satellite observations also include projects (still under development) such as the Wavemill mission (Martin et al., 2016), the Wind and Currents Mission (WaCM, Rodriguez et al., 2018), and the Surface Kinematic Monitoring mission (SKIM, Ardhuin et al., 2018), which aim to directly observe ocean surface currents with a high resolution.

We focus on spatial scales smaller than 100 km and time scales smaller than 45 days, which are the scale ranges where KE associated with BMs and IGWs can be similar (Rocha, Chereskin, et al., 2016; Rocha, Gille, et al., 2016). Our study takes advantage of the unique global simulation mentioned before to analyze the different surface fields in the frequency-wave number space, in all regions of the Global Ocean at two different periods, January–February–March and August–September–October, corresponding to winter and summer (depending on the hemisphere considered). The next section describes the numerical simulation as well as the methodology used to partition motions into BMs and IGWs from the frequency-wave number spectrum. The third section analyses the characteristics of the frequency-wave number spectrum of the six surface fields in terms of the impacts of BMs and IGWs and how these impacts vary seasonally in the Kuroshio–Extension. The fourth section further analyses the geographical and seasonal variations of the impacts of BMs and IGWs on the different surface fields in the World Ocean.

Results of this study are based on the analysis of 12,000 frequency-wave number spectra, corresponding to two seasons, six surface variables (KE, SSH, RV, DIV, SST, and SSS) in one thousand boxes in the world ocean, each box with a $\sim 6^{\circ}$ in latitude size (Figure 2). This constitutes an Atlas containing a wealth of dynamical information that cannot be reported in just one paper. So we feel this Atlas should be freely shared. It will be available on: ftp://ecco.jpl.nasa.gov/ECCO2/LLC4320/global/spectral_analysis/

2. Methodology

2.1. General Circulation Model

A groundbreaking global ocean and sea ice simulation that represents full-depth ocean process with an unprecedented degree of realism is used to characterize BMs and IGWs (Figure 1). The Massachusetts Institute of Technology general circulation model (MITgcm; Marshall et al., 1997; Hill et al., 2007) was the heart of the numerical simulation implemented on a latitude/longitude/polar cap (LLC) configuration (Forget et al., 2015). The global simulation was divided in 13 square tiles with 4,320 grid points on each side (hereinafter called LLC4320).

The LLC4320 was discretized in an Arakawa-C grid type with horizontal grid spacing of $1/48^{\circ}$, ranging from 0.75 km near the Antarctic to 2.2 km at the equator, and 90 vertical levels with 1-m thickness near surface to better resolve the diurnal cycle and a realistic surface boundary layer. The LLC4320 simulation is initialized from a data-constrained global ocean and sea ice solution provided by the Estimating the Circulation and Climate of the Ocean, Phase II (ECCO2) project (Losch et al., 2010; Menemenlis et al., 2008). At this point,

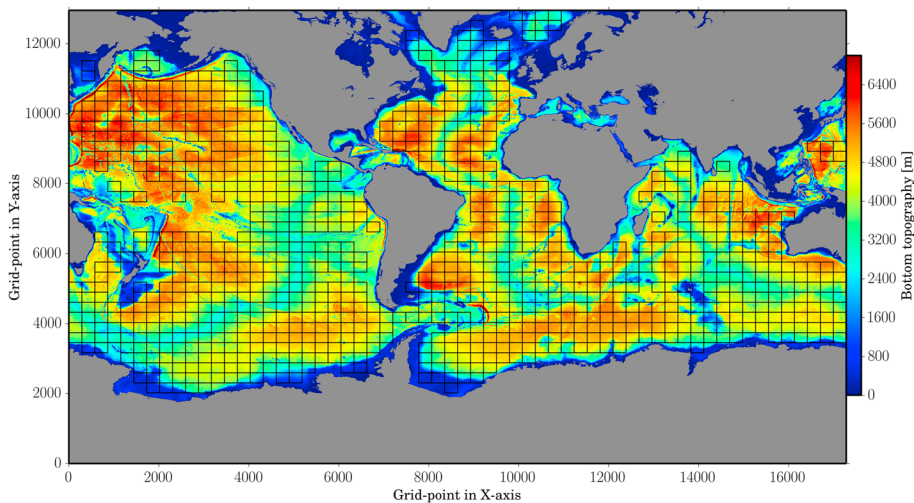


Figure 2. The square boxes used in the spectral analysis. The size of each boxes is 288 grid points $\sim 6^\circ \times \sim 6^\circ$. Boxes with depth less than 200 m as well as those ones containing grid point in land (small islands) were excluded from the analysis.

model resolution was gradually increased to $1/12^\circ$, $1/24^\circ$, and ultimately reach $1/48^\circ$. The numerical configuration is similar through all the LLC simulations except that the LLC4320 includes a synthetic surface pressure field consisting of 16 tidal forcing constituents used to dynamically mimic the tidal forcing (Wang et al., 2018). The six-hourly surface atmospheric fields from the 0.14° (~ 15 km) European Center for Medium-Range Weather Forecasts atmospheric operational model analysis were used as surface boundary conditions. The period of simulation spans from 13 September 2011 to 15 November 2012. The three-dimensional model prognostic variables were saved every 1 hr. More about the setup and instructions of LLC4320 can be found in the following website: http://wwwcvs.mitgcm.org/viewvc/MITgcm/MITgcm_contrib/llc_hires/llc_4320/.

Figure 1 shows a snapshot of surface speed in the global ocean. The coexistence of mesoscale and submesoscale eddies and currents along with internal gravity waves is observable in the snapshot. On one hand, motions in the western boundary currents are well organized and stronger, populated by eddies with a weak IGW signature. On the other hand, motions are diffuse and slow in the eastern boundary currents. The equatorial band is always characterized by the presence of equatorial instabilities and IGWs. The space-time resolution helps to fully resolve MBMs and a large part of SBMs (Rocha, Gille, et al., 2016). In addition, the inclusion of tides provides a conversion of tidal energy into the internal wave field through, both, flow-topography interactions and wave-BM interactions (Arbic et al., 2008).

The LLC4320 simulation has been compared to in situ observations in order to assess the fidelity of the model to reproduce the spectral dynamics and the kinetic energy level at different time and spatial scales. For instance, in terms of spectral dynamics, Rocha, Chereskin, et al. (2016) performed a one-dimensional Helmholtz decomposition (Bühler et al., 2014) of the Acoustic Doppler Current Profiler (ADCP) data and the LLC4320 outputs in the Drake Passage. The model data compared well with the ADCP data for both the rotational and divergent components. Wang et al. (2018), analyzing 25 repeat ADCP surveys in the Northwestern Pacific Ocean and comparing these data with the LLC4320 outputs, concluded the simulation well reproduces the location and amplitude of the kinetic energy peaks revealed by the ADCP surveys. Savage, Arbic, Alford, et al. (2017) tested the performance of two global ocean simulations (using the HYbrid Coordinate Ocean Model [$1/24^\circ$] and the MITgcm [LLC4320]) against nine McLane profilers in the Northern Pacific Ocean. The test focused on the model performance to reproduce the diurnal, semidiurnal, and supertidal variance of SSH. Both models agree with observations at diurnal and semidiurnal tidal ranges, but discrepancies are found at supertidal frequencies (i.e., the IGW continuum). The SSH variance in LLC4320 was closer to the variance displayed by the profilers because of its higher spatial resolution (Mueller et al., 2015). Thus, despite the fact that LLC4320 is a free-running simulation, its higher spatial resolution allows to better reproduce the energy transfer out of the inertial and semidiurnal bands and therefore to realistically reproduce the IGW continuum.

In the subsequent analysis, we used hourly snapshots of surface global maps of several scalar quantities: KE, RV, DIV, SSH, SST, and SSS. These quantities are used to discriminate the impacts of IGWs and BMs through a spectral analysis.

2.2. Partitioning Motions Into IGWs and BMs Using Frequency-Wave Number Spectra

Identification of the respective impacts of IGWs and BMs on the six different fields is based on a spectral analysis in the frequency (ω) and wave number (k) domains. The LLC4320 global ocean simulation has been divided into square boxes with a $\sim 6^\circ$ in latitude size for the two seasons (January–February–March [JFM] and August–September–October [ASO]). This allows to resolve length scales from 4 to 300 km and periods from 2 hr (hourly outputs were used) to 45 days. One thousand boxes (Figure 2) have been used for the spectral analysis (boxes with depths less than 200 m were excluded). This represents a total of 12,000 ω - k spectral Before computing the ω - k spectrum for a given variable in each box, the linear trend in space and time was removed and the three-dimensional dataset (three-month blocks, $\phi(x, y, t)$, where ϕ is an arbitrary variable) was multiplied by a three-dimensional (x , y , and t) Hanning window (Qiu et al., 2018). Afterward, a discrete three-dimensional Fourier transform was computed ($\hat{\phi}(k, l, \omega)$, where k is the zonal wave number, l is the meridional wave number, and ω denotes frequency). Finally, the three-dimensional Fourier transform is used to compute a two-dimensional spectral density, $|\hat{\phi}|^2(k, \omega)$, where k is the isotropic wave number defined as $k = \sqrt{k^2 + l^2}$. The transformation from an anisotropic spectrum to an isotropic spectrum was performed following the methodology described by Savage, Savage, Arbic, Alford, et al. (2017). Briefly, the isotropic wave number vector k is defined as an evenly distributed set of wave numbers. Posteriorly, the three-dimensional Fourier ($\hat{\phi}(k, l, \omega)$) transform is azimuthally averaged over all values of the vector k , and this process was performed iteratively at each element of ω . One concern is about the size of the boxes ($\sim 6^\circ$). Qiu et al. (2017) tested the assumption using the eddy anisotropic ratio (variance of the strain field divided by the eddy kinetic energy), and they found a small ratio at wavelengths ranging 5–100 km. In our study we focused on the 10- to 100-km scale range, such that the flow can be considered isotropic, in which case one can exploit the link between one-dimensional and isotropic two-dimensional spectra (Bühler et al., 2014; Kelly & Wyngaard, 2006).

The dispersion relation curves for IGWs (Gill, 1982) have been also estimated for each vertical normal mode. This required first to estimate the local buoyancy frequency using the vertical temperature and salinity profiles averaged in each box (for each season). Solving a classical Sturm-Liouville problem (Gill, 1982) produced the different Rossby radii of deformation and therefore the related dispersion relation curves as linear functions of ω and k . We found that the curve related to the tenth baroclinic vertical mode (corresponding to the highest baroclinic mode resolved in the simulation) is the most relevant one to partition motions into BMs and IGWs. To better compare the part of the variance explained by IGWs and BMs in different areas of the ω - k space, the spectra have been multiplied by ω and k . In others words, all ω - k spectra shown in this paper are presented in variance preserving form. The error bar shown in wave number spectra and frequency spectra were computed following a classical methodology as used by Rocha, Chereskin, et al. (2016), Rocha, Gille, et al. (2016), and Qiu et al. (2017).

Using the dispersion relation curve for IGWs corresponding to the tenth baroclinic mode, highlights two distinct regions in the ω - k spectra (see Figure 3: schematic of the frequency-wave number spectrum of KE with, both, the frequency [left] and wave number [top] spectra). This methodology is used in Savage, Savage, Arbic, Alford, et al. (2017) and Qiu et al. (2018). As already mentioned, the region above this curve (that includes mostly frequencies equal to or higher than f) exhibits discrete beams aligned with the dispersion relation curves of the different baroclinic modes. These discrete bands above the tenth baroclinic mode suggest weakly nonlinear interactions and that these motions are mostly captured by IGWs (Rocha, Chereskin, et al., 2016; Savage, Savage, Arbic, Alford, et al., 2017). Three additional horizontal bands with frequencies close to tidal (semidiurnal and diurnal) and inertial frequencies span a larger range in the small scales band. The region below the tenth dispersion relation curve, with smaller frequencies, has energy continuously spread out in the ω - k space, suggesting strong energy exchanges through nonlinear interactions. Motions in this region can be associated with BMs that include MBMs and SBMs. It is worth mentioning that the motions in this part of the spectrum do not follow any dispersion relation. Instead, the energy distribution follows a nondispersive line, $\omega - ck = 0$ (where c is the phase speed of mesoscale eddies), meaning that

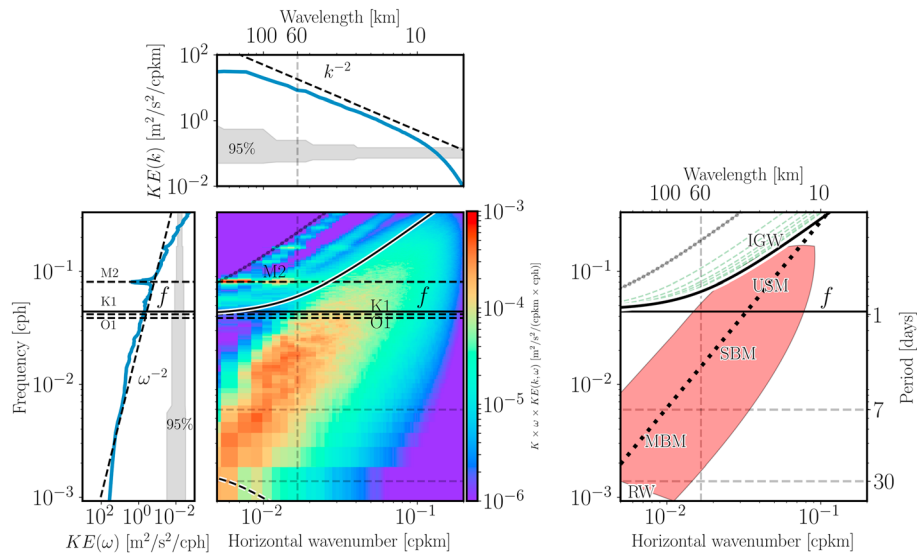


Figure 3. Frequency-wave number spectra of KE ($KE \text{ [m}^2/\text{s}^2\text{]}$) corresponding to the Kuroshio-Extension, during the January–February–March season. The spectrum is multiplied by k and ω , indicating the spectrum is variance preserved. Right panel is the frequency spectrum; upper middle panel is the wavenumber spectrum; bottom middle panel is the frequency-wave number spectrum; left panel is the schematic frequency-wave number spectrum. The schematic spectrum displays the multiple dynamical regimes: RW stands for Rossby waves, MBM for mesoscale balanced motions, SBM for submesoscale balanced motions, USM for unbalanced submesoscale motions, and IGW for internal gravity waves. Additionally, the schematic spectrum shows the dispersion relation of the first ten baroclinic modes: mode-1 in gray dotted line, mode-2 to mode-9 green dashed lines, and mode-10 in black. Finally, the *nondispersive line*, $\omega - ck = 0$, is drawn with c corresponding to an eddy speed of 8.5 km/day (~ 10 m/s). Gray band in right and upper panels denote the 95% confidence intervals.

the motions within this region do not belong to the wave dynamics. Integrating this ω - k spectrum over the k range or ω range allows to recover respectively the frequency spectrum or the wave number spectrum, respectively, as sketched in Figure 3.

This clearly emphasizes that the ω - k spectrum well allows to identify the BM and IGW dynamical regimes (or to diagnose the partition of motions into BMs and IGWs) by using the dispersion relation curve associated with the tenth baroclinic mode (this means we do not consider the variance in the tidal and inertial bands and with k larger than the one given by the dispersion relation curve associated with the tenth baroclinic mode). This variance has been found to be negligible. This is the criterium used in the next section.

In section 4, we focus on scales smaller than 100 km since, from section 3, these are the scales where the BM and IGW impacts are almost similar. Consequently, in this section, for a given range of spatial scales, the variance above the dispersion relation curve for IGWs corresponding to the tenth baroclinic mode has been associated to IGWs and the one below this curve associated to BMs. Two scale ranges are considered: 10–50 km (that concern SBMs) and 50–100 km (called MBMs). Using the ω - k spectra, we have estimated for each scale range the ratio, R , between the variance associated with BMs and that associated with IGWs as: $R = \frac{\text{BM variance}}{\text{IGW variance}}$. So for a given spatial-scale band and a given variable, $R > 1$ means that the variability of the flow is explained by BMs and $R < 1$ means the variability of the flow is explained by IGWs.

3. Analysis of the Frequency-Wave Number Spectra for the Different Fields in the Kuroshio-Extension Region

In this section, we exploit the information provided by the ω - k spectrum analysis to better understand the respective impacts of BMs and IGWs on the different surface fields. We focus on the KE, SSH, and SST fields in the Kuroshio-Extension region. The corresponding winter and summer spectra shown on Figures 4a–4i unveil how each field differs from the other in terms of the partition of motions into between BMs and IGWs.

First, figures displaying the ratio between winter and summer variances for KE and SSH (Figures 4c and 4f) remarkably confirm the choice of the dispersion relation curve associated with the tenth vertical normal

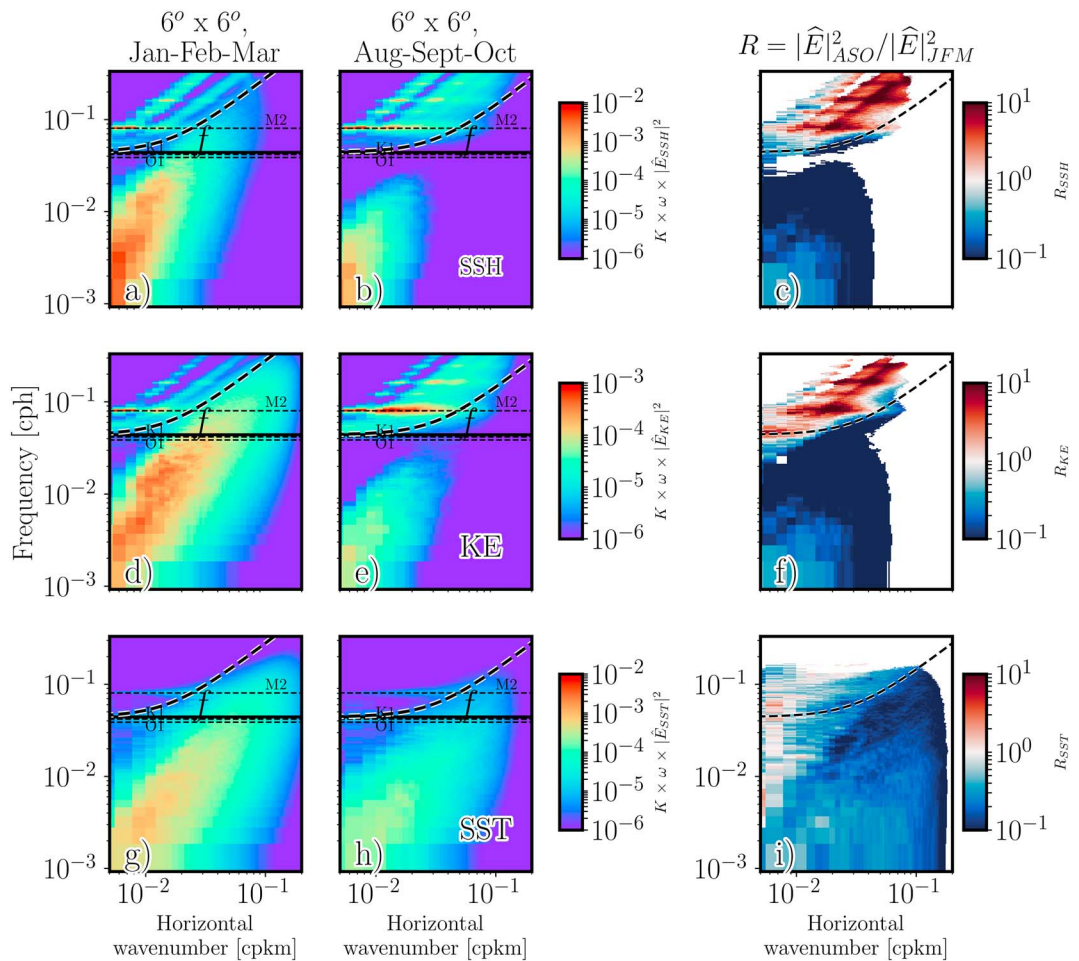


Figure 4. Frequency-wave number spectra for sea surface height (m^2), kinetic energy (m^2/s^2), sea surface temperature ($^{\circ}\text{C}^2$) in the Kuroshio-Extension region in January–February–March (JFM) and August–September–October (ASO) months. The third column represents the ratio of the spectrum in ASO over the spectrum in JFM. The first two columns display the dispersion relation of mode 10 in JFM and ASO, respectively. The third column displays the dispersion relation of mode 3.

mode to discriminate IGWs from BMs. IGWs discriminated that way are clearly more energetic in summer, whereas BMs (mostly SBMs, i.e. <50 km) strongly dominate in winter. Note that a signature of internal tides M_2 is present on the SSH and KE field over a large range of wave numbers in summer.

Second, in terms of IGW impacts, SST (like SSS not shown) displays dramatic differences with SSH and KE. IGW impacts just do not show up in the SST field (Figures 4g–4i), except for IGWs with M_2 and f frequencies. But IGWs do have a significant impact on SSH and KE as displayed by the discrete beams above the tenth vertical normal mode curve (Figures 4a–4f). One way to explain these differences is to invoke IGW characteristics. SST and SSS are horizontally advected by surface motions, including IGWs that are oscillating with periods related to their frequencies. IGWs with frequencies higher than the inertial frequency, f (~ 18 hr), have usually horizontal velocity magnitudes not larger than 0.1 m/s. This means that the largest horizontal displacement of SST and SSS by these waves, within half the inertial period, will be smaller than 4 km. Since the smallest length scale resolved by our simulation is 4 km, these IGW motions cannot show up in the SST and SSS fields.

Third, as mentioned before, SBMs (<50 km) are much more energetic in winter than in summer in the three fields (SST, SSH, and KE). But a remarkable characteristic, new to our knowledge, is the emergence of a significant submesoscale contribution for frequencies larger than f during winter. This contribution has almost the same order of magnitude as the one for smaller frequencies. This is particularly true for the SST and KE fields. In the subsequent analysis, we refer the related submesoscale motions as unbalanced submesoscale motions (USMs, see the schematic spectrum in Figure 3). Importance of USMs will be addressed in a future study.

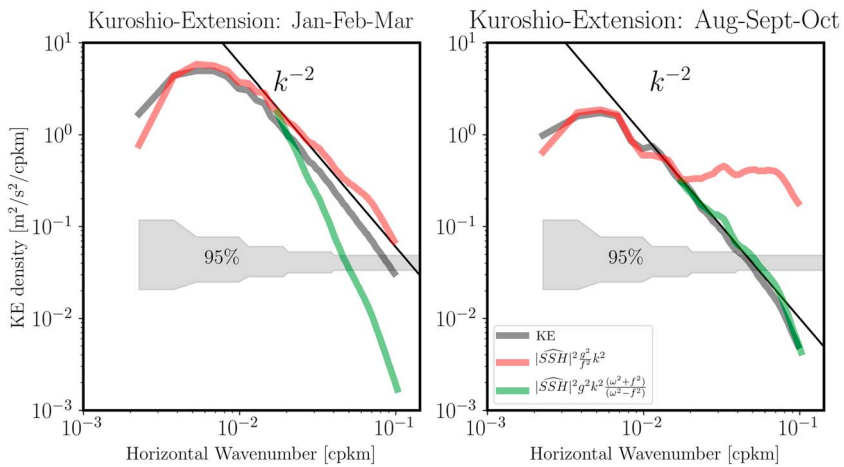


Figure 5. Wave number spectra of kinetic energy ($m^2/s^2/(cpkm)$) deduced from (u, v) (gray line), and from sea surface height (geostrophic kinetic energy; red line), and the kinetic energy of internal gravity waves (green line). The shaded gray bands denote the 95% confidence interval.

Further analyzing these ω - k spectra allows to unveil and better understand some other IGW and BM impacts in terms of variance. They are discussed in the next two sections.

3.1. Different Impacts of IGWs and BMs on KE and SSH

We first focus on the KE and SSH spectra to better understand the different IGW impacts on these fields, after the results from Rocha, Gille, et al. (2016) and Qiu et al. (2018). Whereas KE wave number spectrum estimated from SSH, using the geostrophic approximation, (red curve on Figure 5a) and the KE spectrum estimated from surface motions (gray curve on Figures 5a) do not display any spectral slope discontinuity in winter, the same spectra in summer (Figure 5b) reveal conspicuous differences. More precisely, the KE spectrum from SSH (red curve on Figure 5b) exhibits in summer a conspicuous slope discontinuity separating a k^{-2} slope for large scales from a flat slope for smaller scales. The length scale associated with this discontinuity is ~ 50 km. Such slope discontinuity is not observed on the KE spectrum from surface motions (gray curve on Figure 5 b). These results, similar to those reported in Rocha, Gille, et al. (2016) and Qiu et al. (2018), are consistent with the ω - k spectra on Figures 4c and 4f, indicating that in summer, IGWs much more dominate the SSH field than the KE field for scales < 50 km. Considering SSH as a proxy for potential energy (PE), this suggests these conspicuous differences between KE and SSH spectra in summer should be explained in terms of the relationship between PE and KE that differs for BMs and IGWs (as detailed in Gill, 1982; see also Qiu et al., 2018). Indeed, using a shallow water model associated with a given vertical normal mode (in that case, PE is directly related to SSH), it can be shown that on one hand, the relationship between KE and PE for BMs in the spectral space (using the geostrophic approximation) is simply given by:

$$\widehat{\text{KE}} = \left| \widehat{\text{SSH}} \right|^2 \frac{g^2}{f^2} k^2, \quad (1)$$

with $\widehat{\text{KE}} = |\widehat{u}|^2 + |\widehat{v}|^2$. On the other hand, the relationship between KE and PE for IGWs is given by (Gill, 1982; Qiu et al., 2018)

$$\widehat{\text{KE}} = \left| \widehat{\text{SSH}} \right|^2 g^2 k^2 \frac{(\omega^2 + f^2)}{(\omega^2 - f^2)^2} = \frac{\left| \widehat{\text{SSH}} \right|^2 \frac{g^2}{f^2} (2 + Rd^2 k^2)}{(Rd^4 k^2)}, \quad (2)$$

when using the dispersion relation curve ($\omega^2 = f^2(1 + Rd^2 k^2)$) of the vertical normal mode considered with Rd its Rossby radius of deformation. Thus, (1) indicates a k^{-2} slope difference between $\widehat{\text{KE}}$ and $\left| \widehat{\text{SSH}} \right|^2$, whereas (2) indicates similar slopes for $\widehat{\text{KE}}$ and $\left| \widehat{\text{SSH}} \right|^2$, at least for large k . To further check this argument, we have

estimated the KE wave number spectrum from SSH using (1) and (2). As displayed by the red curve in Figure 5b, KE estimated from SSH using (1) matches quite well the observed KE spectrum (gray curve) down to a scale ~ 50 km. But a strong discrepancy emerges at smaller scales, suggesting a strong imbalance. However, using (2) for scales smaller than 50 km leads to a KE spectrum from SSH (green curve) quite close to the observed one (gray curve). This good agreement has been actually found by choosing an appropriate vertical mode that corresponds to the third vertical mode. Indeed, choosing a lower (higher) vertical mode leads to underestimate (overestimate) the KE associated to IGWs. Such good agreement using simple equations (1) and (2) related to just the third vertical normal mode was unexpected, and this finding seems to be new to our knowledge. But it is consistent with Figures 4c and 4f discussed before, which emphasize a strong IGW intensification in summer mostly around the third vertical mode (dashed line in Figure 4c, 4f, and 4i; as also discussed by Rocha, Gille, et al., 2016).

For the Kuroshio-Extension region considered in this section, this slope discontinuity in the SSH wave number spectrum concerns the small-scale range (<50 km). Its existence is thus a strong indication of the IGW dominance over SBMs. As such, it can be thought of as one way to discriminate IGWs and SBMs when having access to satellite altimeter observations with a resolution high enough.

No slope discontinuity is present in the KE wave number spectrum, and therefore, the KE spectral characteristics alone cannot help to discriminate IGWs from BMs if an additional analysis is not done (see next section).

3.2. Impacts of IGWs and BMs on the Rotational and Divergent Parts of the Surface Flow Field

We have tested whether methodologies based on the Helmholtz decomposition allow to discriminate BMs from IGWs. The Helmholtz decomposition by itself (through which KE is decomposed into a rotational part [RV] and a divergent [DIV] part, Vallis, 2006) of course does not allow this discrimination since each, BMs and IGWs, have a priori nonzero RV and DV parts. However, some studies using on this decomposition (Bühler et al., 2014) further assume BMs are nondivergent, meaning the total DIV part resulting from the Helmholtz decomposition is entirely explained by IGWs. Then the RV part for IGWs is retrieved from the DIV part for IGWs using a relationship between the relative vorticity and the divergence appropriate for IGW dynamics (see Bühler et al., 2014). The RV part for BMs is finally just the difference between the total RV part (from the Helmholtz decomposition) and the RV part for IGWs. Many studies have used this promising methodology to discriminate BMs from IGWs (Bühler et al., 2014; Qiu et al., 2017; Rocha, Chereskin, et al., 2016). However, SBMs are known to be nondivergent (Klein & Lapeyre, 2009; McWilliams, 2016). But most of the previous studies based on Bühler's methodology assumes this contribution is negligible. Our analysis of the ω - k spectra reveals that these methodologies can be used but with some caveats.

The Helmholtz decomposition makes use of

$$u = -\psi_y + \phi_x, \quad v = \psi_x + \phi_y, \quad (3)$$

with ψ the stream function and ϕ the potential. This leads to

$$\text{RV} = \zeta = v_x - u_y = \Delta\psi \quad \text{and} \quad \text{DIV} = -w_z = u_x + v_y = \Delta\phi. \quad (4)$$

In the ω - k spectral space, the relation between KE, RV, and DIV is

$$\widehat{\text{KE}} = \left| \widehat{\text{RV}} \right|^2 / k^2 + \left| \widehat{\text{DIV}} \right|^2 / k^2. \quad (5)$$

$\left| \widehat{\text{RV}} \right|^2 / k^2$ and $\left| \widehat{\text{DIV}} \right|^2 / k^2$ are called respectively the RV and DIV contributions to KE. Using surface motions from the global numerical simulation, we have first checked that (5) is accurate to machine precision in the ω - k spectral space. Then, we have diagnosed the partition of motions into BMs and IGWs in, both, the RV and DIV contributions by examining their ω - k spectrum shown on Figures 6a–6f. These figures again reveal for both contributions a strong seasonality, with BMs dominating in winter and IGWs more dominant in summer (Figures 6c and 6f).

The winter RV and DIV contributions to KE (Figures 6a and 6b) are dominated by BMs (with MBMs [i.e., >50 km] more dominant than SBMs [i.e., <50 km]). It is interesting to note that for both contributions, USMs are again nonnegligible. IGWs are present in the first and second baroclinic modes for DIV but

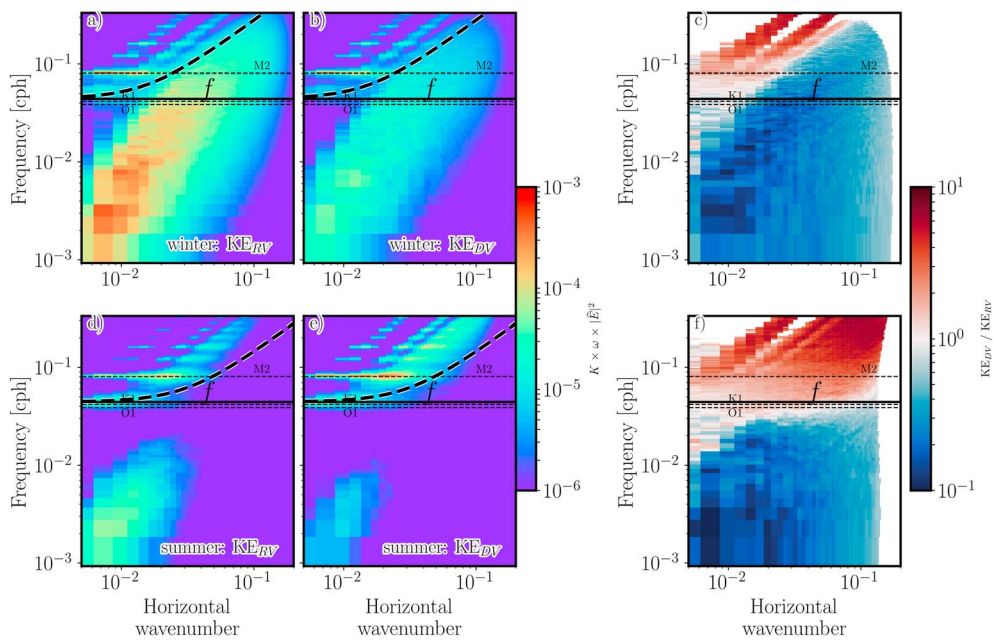


Figure 6. Frequency-wave number spectra for kinetic energy associated with the rotational part of the flow (KE_{RV} [m^2/s^2], a–c) and the divergent part of the flow (KE_{DV} [m^2/s^2], d–f). The ratio divergent over rotational is shown in (c) and (f). The label winter stands for January–February–March, and the label summer stands for August–September–October.

contribute very weakly to the total variance in particular for RV. This means that the assumption of nondivergent BMs used by Bühler et al., 2014 is not necessarily valid for the winter, since the DIV of BMs is nonnegligible. Although, the winter $|\widehat{DIV}|^2 / |\widehat{RV}|^2$ ratio (Figure 6c) further indicates a RV contribution larger than the DIV one for both MBMs and SBMs; however, this cannot be the case for other regions in the World Ocean.

The summer RV and DIV contributions to KE (Figures 6d and 6e) totally differ from winter ones. As expected, SBMs just do not show up in these summer fields (Figures 6d and 6e), and MBMs are much weaker than in winter. The IGW part contributes much to the summer RV contribution and is centered around the third baroclinic mode. M_2 internal tides are intensified in the 50- to 100-km band. The DIV contribution is even much more dominated by IGWs than the RV one, with again an intensification around the third vertical mode as well as in the M_2 frequency in the 50- to 100-km band. The $|\widehat{DIV}|^2 / |\widehat{RV}|^2$ ratio (Figure 6f) clearly indicates that in summer, the diurnal (O1, K1) frequency separates lower frequencies for which BMs dominate from higher frequencies for which IGWs dominate, which justifies using the daily average operator to separate BMs from IGWs. It also confirms that using the Bühler et al. (2014) assumption is appropriate in summer.

To further relate these results with those from previous studies that mostly consider wave number spectra, we have plotted the wave number spectra of the RV and DIV contributions after integrating $|\widehat{RV}|^2(\omega, k)/k^2$ and $|\widehat{DIV}|^2(\omega, k)/k^2$ over all the frequencies. These spectra, shown on Figures 7a and 7b, confirm the previous comment, indicating that in winter, the RV contribution explains most of the KE, except for the small-scale range where RV and DIV contributions are close. The spectral slope of the RV contribution in winter is similar to that for KE and close to k^{-2} as expected in this region in winter (as found in Sasaki et al., 2014; Rocha, Gille, et al., 2016). Results much differ in summer. Whereas RV contribution to KE explains most of the KE for larger scales (>70 km), DIV contribution mostly explains KE for smaller scales, in particular those smaller than 50 km. The KE spectral slope is still close to k^{-2} in summer. But when excluding IGWs, that is, retaining only the RV contribution (since IGWs mostly explain DIV contribution during this season and are quite weak in the RV contribution), the slope is in k^{-3} (as also found in Sasaki et al., 2014, using daily averaged fields).

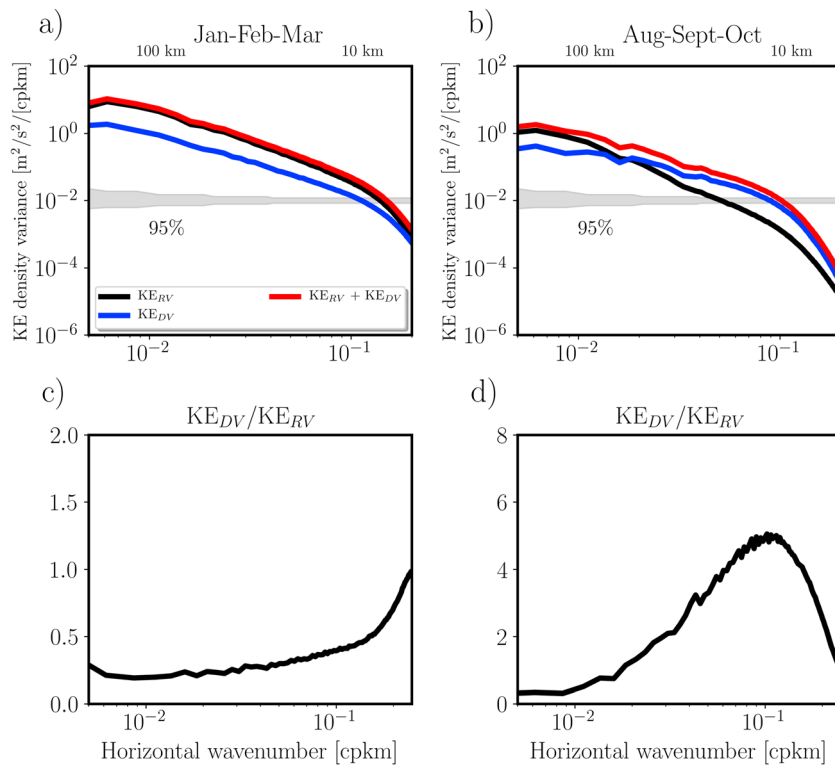


Figure 7. Wave number spectra contribution of relative vorticity (RV) and divergent (DIV) to kinetic energy (KE; m^2/s^2 (cpkm)). The ratio divergent over rotational is shown in the lower panels. The shaded gray bands denote the 95% confidence interval.

This conspicuous discrepancy between RV and DIV in summer contributions further appears when examining the ratio $|\widehat{\text{DIV}}|^2 / |\widehat{\text{RV}}|^2$ as a function of k alone. This ratio (shown on Figures 7c and 7d) is often used to understand whether horizontal motions are balanced or unbalanced (McWilliams, 2016). The ratio in winter (Figure 7c) is close to 0.25 for large scales, increases much in the small-scale range, but does not become larger than one for the largest k . This suggests that the flow is mostly balanced, which is consistent with the fact that the DIV contribution is dominated by SBMs. Results much differ in summer (Figure 7d). Although still close to 0.25 for large scales ($>100 \text{ km}$), it increases and attains one at scale of 50 km, still indicating balanced motions. But it further increases again for smaller scales to attain a maximum of five at a scale of 10 km. Such values, larger than one, indicate unbalanced motions. But these motions are mostly IGWs since the summer DIV contribution is dominated by IGWs. These large ratios can be easily rationalized using the relationship between RV and DIV for linear IGWs. It simply writes

$$\frac{|\widehat{\text{DIV}}|^2(k)}{|\widehat{\text{RV}}|^2(k)} = \frac{\omega^2}{f^2} = 1 + R d^2 k^2, \quad (6)$$

using again the dispersion relation related to a given mode. Thus, the ratio increases as k^2 . It is noteworthy that the DIV contribution decreases at scales smaller than 10 km due to impact of numerical diffusivity.

One last remark is that preceding results also indicate that whereas RV variance is much larger in winter than in summer, DIV variance does not change much seasonally, as emphasized by RV and DIV spectra in summer and winter on Figures 7a and 7b (and also found by Rocha, Gille, et al., 2016, looking at the time series). This similar DIV magnitude in summer and winter is actually due to the dominant SBM impact in winter and the IGW impact in summer. As explained by Rocha, Gille, et al. (2016), intensification of the IGWs in summer is due to the larger magnitude of baroclinic mode-3 because of shallower mixed layer. Since DIV is associated with

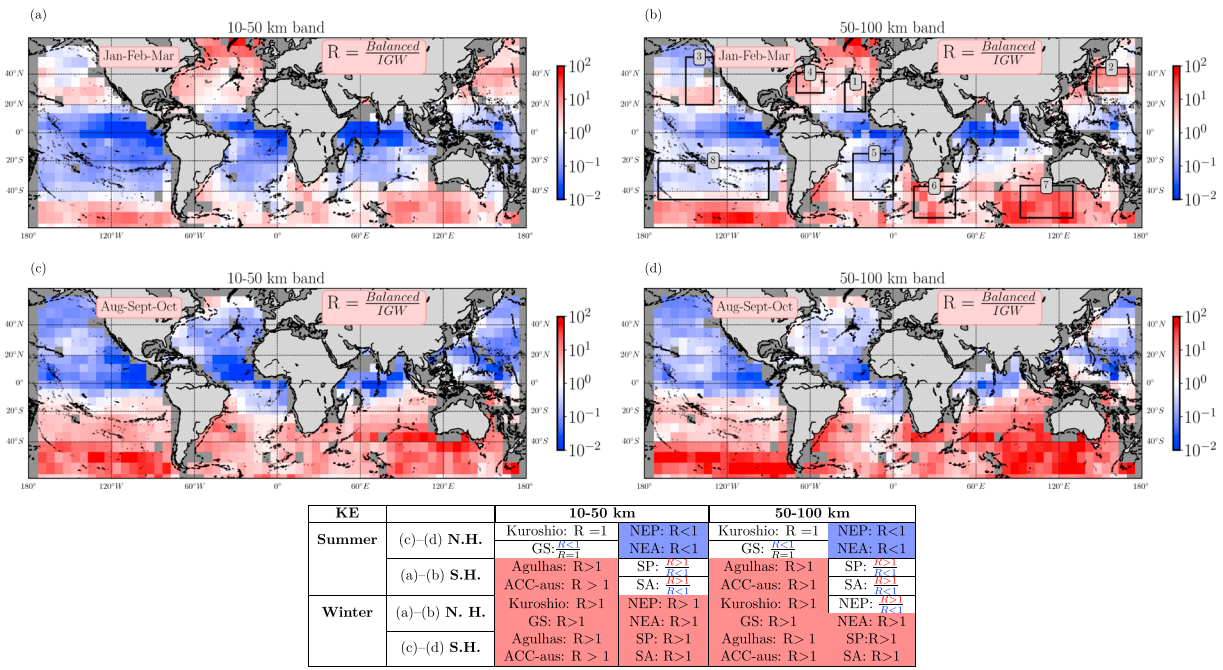


Figure 8. Global maps of the ratio R (balanced motion [BM]/internal gravity waves [IGW]), for kinetic energy: (a and b) January–February–March (winter Northern Hemisphere); (c and d) August–September–October (summer Northern Hemisphere). The lower table displays the R values for the targeted areas displayed in Figure 1. R values shown as fraction indicate that such regions are highly heterogeneous.

vertical velocity, using an appropriate methodology to partition motions into IGWs and BMs has important consequences when we want to access to vertical fluxes of any quantities. Indeed, IGWs are known to have almost no explicit impacts on these fluxes, the latter being mostly explained by BMs and in particular by SBMs. The preceding results indicate that Bühler et al. (2014) method, which assumes IGWs mostly explain the DIV contribution, should be fine in summer but inaccurate in winter. In addition, they reveal that a wealth of information can be obtained using the Helmholtz decomposition.

These results for the Kuroshio-Extension region discussed in the previous two sections reveal how using the ω - k spectrum of the different fields allows to unveil and better characterize the relative impacts of IGWs and BMs on these fields. These impacts strongly differ from one field to the other and are seasonal dependent, with IGWs becoming significant during summer principally for scales smaller than 50 km for both SSH and KE. Can these results be extended to other regions of the world ocean? This strongly depends on the relative contribution of BMs and IGWs. The next section investigates this partition of motions into between IGWs and BMs in the different surface fields for the World Ocean in terms of the ratio R (defined in section 2) and how these impacts compare with those in the Kuroshio-Extension region.

4. Geographical Distribution of IGWs and BMs in the World Ocean

We now explore, in the World Ocean, the geographical and seasonal impacts of IGWs and BMs with scales smaller than 100 km. The different surface fields considered include the KE, SSH, RV, and DIV as well as the SST and SSS fields. As described in section 2.2, the partition of motions into IGWs and BMs is diagnosed in terms of R values (the ratio between the variance associated with BMs and that associated with IGWs) with respect to 1. This diagnosis is done for two wave bands, the 50- to 100- and 4- to 50-km bands, by making use of the ω - k spectra of the six different fields estimated in each of the one thousand boxes in summer and winter (Figure 2).

Results displayed on Figures 8–12 emphasize that some characteristics already pointed out in the Kuroshio-Extension region (section 3) extend to the World Ocean. First, all the oceans experience a strong seasonality of this partition, with IGWs more dominant in summer and BMs (mostly SBMs) in winter. This concerns all fields, except for the SST (Figure 12) and SSS (not shown) fields on which IGWs have almost no impact as

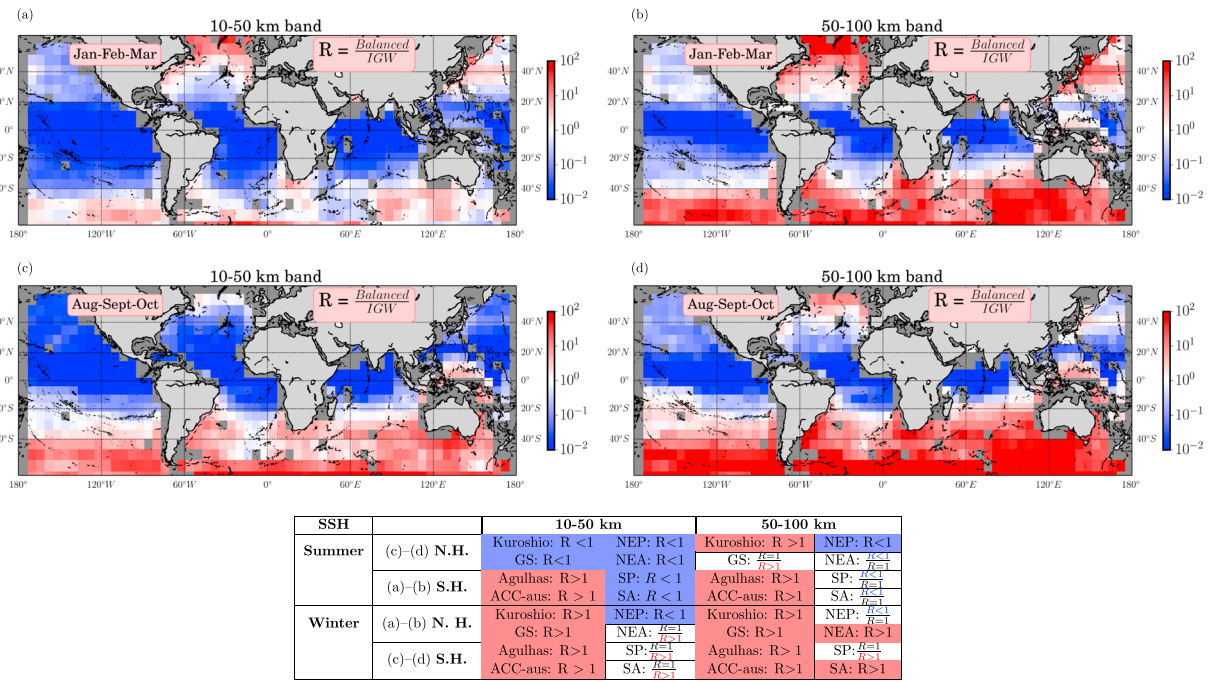


Figure 9. Same as Figure 8 but for sea surface height.

for the Kuroshio-Extension region. Second, the differences between SSH and KE already discussed in section 3.1 are ubiquitous in the World Ocean: in regions where IGWs are already dominant ($R < 1$) in the KE field, SSH is even more affected by IGWs ($R \ll 1$). Third, using the RV and DIV fields (Figures 10 and 11), results further indicate the assumptions used in methodologies based on the Helmholtz decomposition may work only during summer. Fourth, in most of the regions, results do not reveal any particular differences between the two wave bands for the four fields, KE, SST, SSS, and RV. Only the SSH and DIV

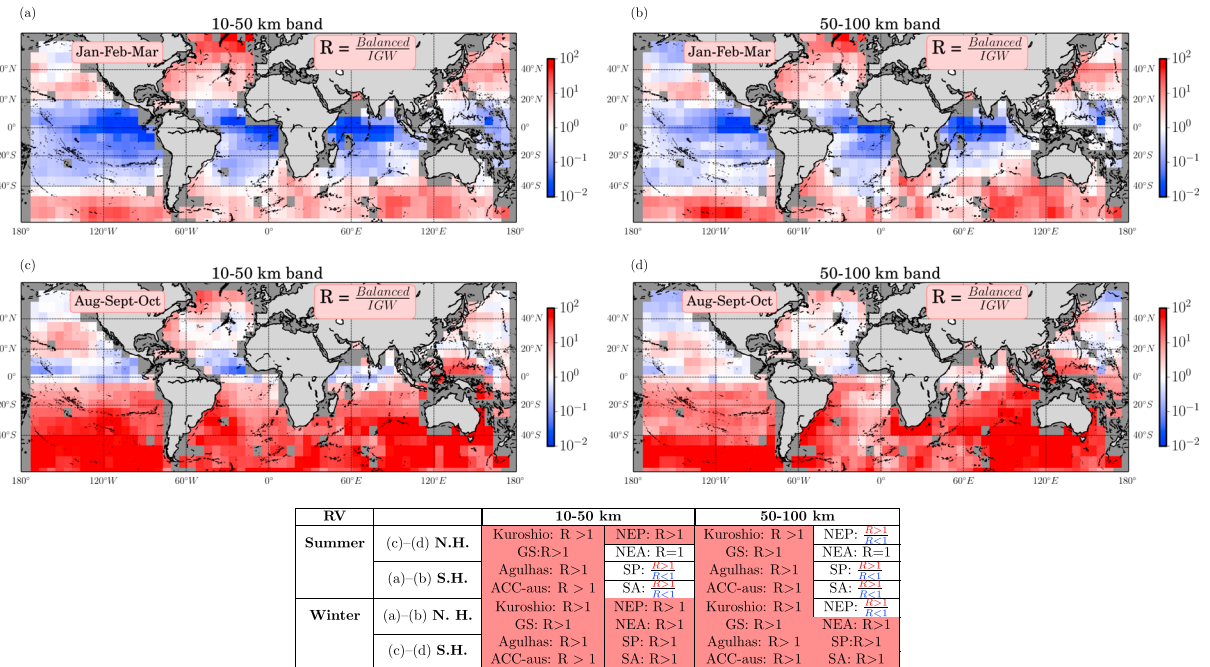


Figure 10. Same as Figure 8 but for surface relative vorticity.

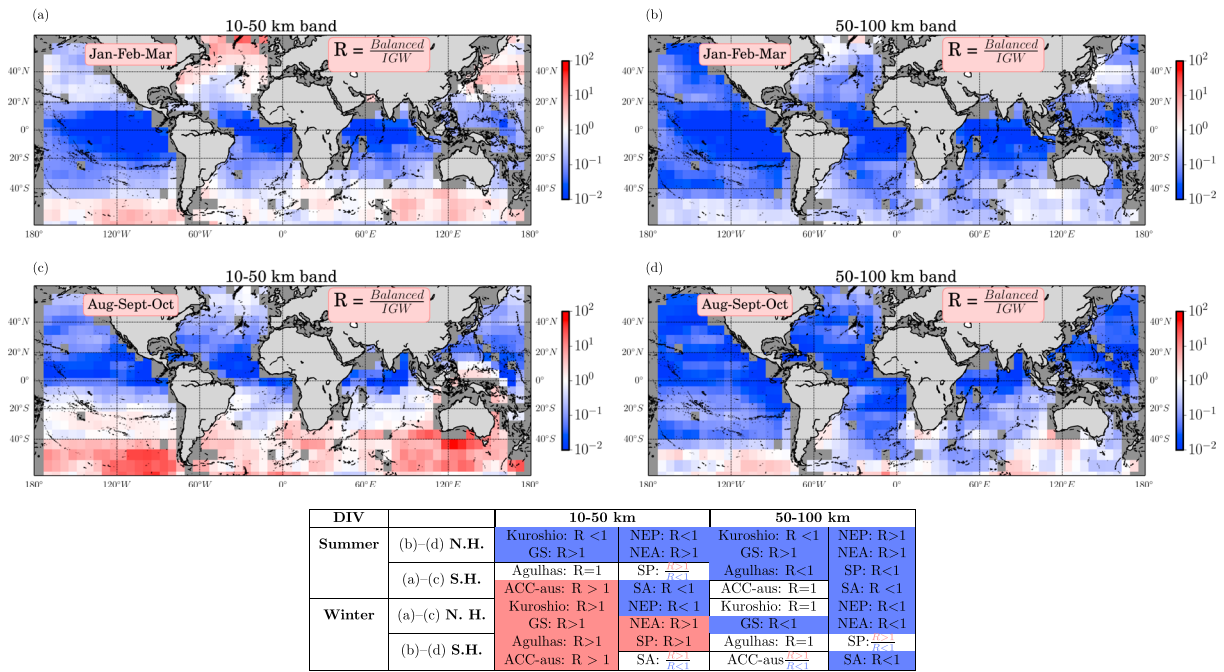


Figure 11. Same as Figure 8 but for surface divergence.

fields do exhibit strong differences with scales smaller than 50 km much more impacted by IGWs than larger scales as already found in the Kuroshio-Extension region.

When analyzing all the oceans in the world, one new result (from Figures 8–12) concerns the significant differences between the two hemispheres. Northern oceans are more affected by IGWs than southern oceans. As a consequence, northern oceans display a larger seasonality in terms of IGW and BM impacts than southern oceans. A second new result is that in each hemisphere, a strong regional heterogeneity in the partition of

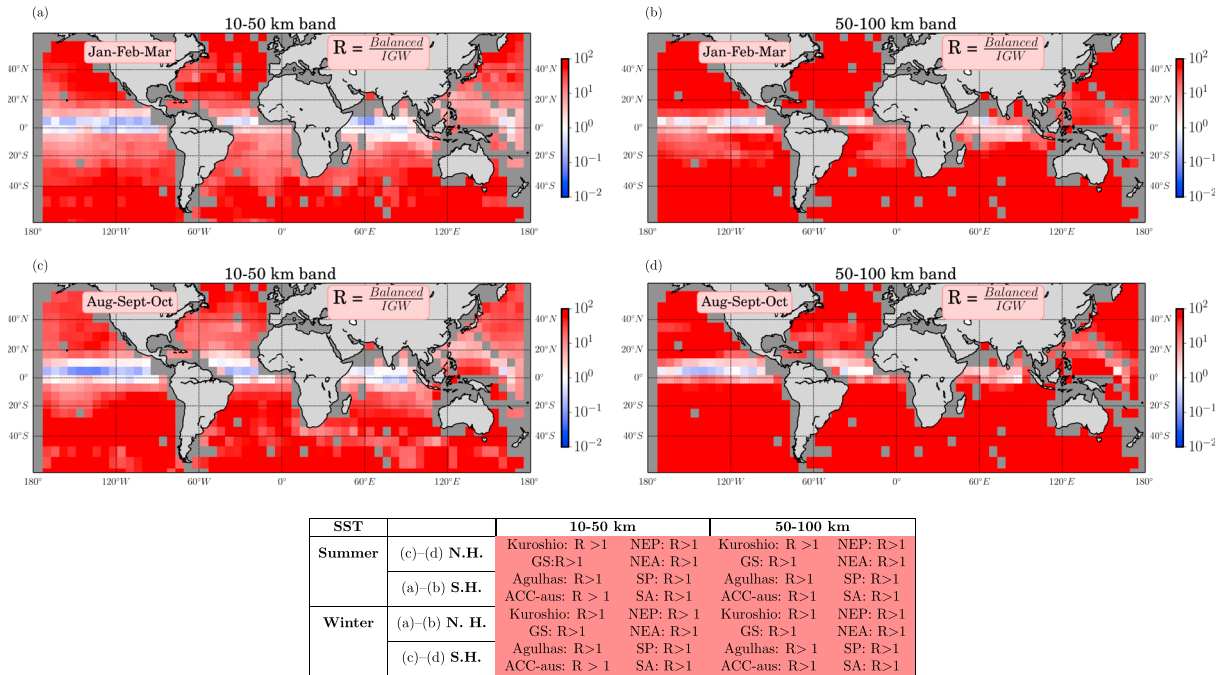


Figure 12. Same as Figure 8 but for sea surface temperature.

motions into IGWs and BMs is observed. Not surprisingly, IGWs are more dominant in low EKE regions than in high EKE ones (such as the Kuroshio-Extension region). To better emphasize this heterogeneity, we have considered four specific regions (two high and two low EKE regions) in each hemisphere. As identified on Figure 1, high EKE regions concern: the Kuroshio-Extension (KEx) and the Gulf Stream regions in the Northern Hemisphere and the Agulhas (AG) and the Antarctic Circumpolar Current (ACC) close to Australia (ACC-AUS) for the Southern Hemisphere. Low EKE regions concern the Northeast Pacific (NEP) and Northeast Atlantic (NEA) regions in the Northern Hemisphere and the South Pacific (SP) and South Atlantic (SA) regions for the Southern Hemisphere. The next sections detail these results for the World Ocean.

4.1. Differences Between Northern and Southern Hemispheres

The KE in the Northern Hemisphere is remarkably more impacted by IGWs than the Southern Hemisphere, with these differences essentially emerging in summer as summarized in the Table of Figures 8. This indicates that a part of what was found previously for the Kuroshio-Extension region in summer cannot be extended to the Southern Hemisphere.

In the Northern Hemisphere in summer (Figure 8, panels c, d), high EKE regions are almost equally impacted by IGWs and BMs with a slighter larger BMs dominance in the 50–100-km band and a slight IGWs dominance in the 10- to 50-km band. The situation much differs for low EKE regions of this Hemisphere in summer: IGWs strongly dominate the KE field for both wave bands (10–100 km) in the NEP and the NEA. IGWs have a much weaker impact in the Southern Hemisphere in summer (Figures 8a and 8b): KE field in high EKE regions (Agulhas (AG) and ACC close to Australia (ACC-AUS)) is strongly dominated by BMs whereas in low EKE regions (SP and SA), BMs slightly dominate or equal IGWs. However, in, both, Northern and Southern Hemispheres in winter, the KE field in most of all regions of the World Ocean (Figure 8) is more affected by BMs than by IGWs, with this, again, concerning the two wave bands. Only the NEP in the 50- to 100-km wave band is almost equally affected by BMs and IGWs (see Table in Figures 8).

These winter/summer differences emphasize the seasonal contrasts in terms of the partition of motions into IGWs and BMs, with these contrasts affecting much more the Northern Hemisphere than the Southern Hemisphere, indicating larger IGW impacts during summer in the Northern Hemisphere. The NEP region (NEA) is the region of the world ocean the most affected by IGWs.

One explanation for these strong differences between the two summer hemispheres can be expressed in terms of the energy associated with internal tides. Internal tides (including diurnal and semidiurnal tides) as well as their harmonics with smaller scales (supertidal motions) are mostly energetic in the latitude band between 30°S and 30°N as pointed out by Savage, Arbic, Richman, et al. (2017, Figures 12 to 16). However, as emphasized by these authors, internal tides and their harmonics in the Northern Hemisphere are still energetic outside this latitude band, but much less in the Southern Hemisphere. Thus, north of 30°N, these energetic tidal motions are found principally in most of the North Pacific Ocean and also in the Gulf Stream and Azores regions (Savage, Arbic, Richman, et al., 2017). South of 30°S, these tidal motions are found only in small areas located in southeast of Australia, in the Drake passage, east of the Agulhas Current, in the Kerguelen plateau, and in the South Atlantic Ocean (Savage, Arbic, Richman, et al., 2017). Near-inertial motions, the other dominant class of IGWs, are also more energetic in the Northern Hemisphere than in the Southern Hemisphere (Chaigneau et al., 2008). In Northern Hemisphere, this mostly concerns the whole North Pacific Ocean and the Western part of the North Atlantic Ocean (see Figure 1 in Chaigneau et al., 2008). In Southern Hemisphere, the near-inertial KE is only 65% the one in the Northern Hemisphere (Figure 3 in Chaigneau et al., 2008). Additionally, the mixed layer has direct consequences on the surface variability of IGWs. Qiu et al. (2018) shown that the Southern Hemisphere mixed layer is deeper than in the Northern Hemisphere, such deeper mixed layer instigates unfavorable conditions for surface trapping of IGWs.

4.2. Differences Between SSH and KE

Results found for the Kuroshio-Extension in terms of IGWs and BMs impacts on SSH and KE extend to some regions of the World Ocean during summer as revealed by the comparison of Figures 8 with Figures 9. This mostly concerns high EKE regions of the Northern Hemisphere and low EKE regions of the Southern Hemisphere. In other regions, IGWs and BMs impacts on SSH and KE exhibit different characteristics.

In the high EKE regions of the Northern Hemisphere (i.e., not only the Kuroshio-Extension but also the Gulf Stream) in summer, IGWs impact more on the SSH field than the KE field (in terms of the ratio R) in the 10-

to 50-km band. But the partition of motions into BMs and IGWs in the 50- to 100 km wave band in this hemisphere during this season does not vary much between KE and SSH, as emphasized by the comparison of Figures 8 and 9 and their tables. In the low EKE regions of this hemisphere in summer, IGWs, which already dominate the KE field in the 10- to 100-km band, have an even larger impact on the SSH field (in terms of the ratio R) over all this scale band (Figures 8 and 9).

In summer of the Southern Hemisphere, in the low EKE regions (SP and SA), IGWs have more impacts on the SSH field than on the KE field and this concerns only the 10- to 50-km band (Figure 9a). But in high EKE regions (AG and ACC-AUS) during this season, SSH as KE is not affected by IGWs, as emphasized by the comparison of tables on Figures 8 and 9.

In winter, the SSH field in all high EKE regions of both hemispheres are dominated by BMs (for both wave bands). However, during this season, SSHs in low EKE regions in both hemispheres (NEP and NEA as well as SP and SA) are still more affected by IGWs than KE, in particular for the 10- to 50-km band. Again, the NEP region displays the strongest contrasts in terms of SSH versus KE, indicating the strong IGW influence there (see tables on Figures 8 and 9).

The results founded in the Kuroshio-Extension explain SSH and KE differences in many regions of the World Ocean. As explained in this section, the IGW impact on SSH stronger than on KE is principally due to the IGW relationship between PE and KE that differs from that for BMs. The consequence is a slope discontinuity in the SSH wave number spectrum, whereas the KE spectrum does not exhibits such discontinuity. Qiu et al. (2018) intensively discussed the critical length scale that separates the scale range where BMs dominate from the one where IGWs dominate. Not surprisingly, this length scale, usually close to 50 km, is similar to the one that characterizes the slope discontinuity for high EKE regions. Richman et al. (2012, Figure 4) in the Kuroshio-Extension, and later on, Rocha, Chereskin, et al. (2016) for the Drake passage found similar results for scales close to 50 km. This slope discontinuity in the SSH spectrum seems to hold in the World Ocean. Indeed, an analysis of the KE and SSH wave number spectra in many regions during summer season (not shown) confirms that the strong slope discontinuity in the SSH spectrum is not observed in the KE spectrum. Furthermore, the SSH spectral slope discontinuity found in low EKE regions (involving a separation length scale larger than 50 km, not shown) is reminiscent from the results from Xu and Fu (2012).

Another remarkable result (from the comparison of Figures 8 and 9) is that in regions where $R > 1$ (indicating a dominance of BMs) in the KE field, this ratio is even much larger in the SSH field (corresponding to a darker red color on Figures 9). This is particularly well observed in the winter Southern Hemisphere in the 50–100 km band (Figure 9d). One plausible explanation is that in winter, near-inertial waves are quite energetic and therefore have an impact on the KE field but not on SSH since these waves are known to have no signature on this field (Gill, 1982).

This significant IGW impact on SSH is a major challenge for SWOT since the geostrophic approximation cannot be used anymore to recover BMs for scales smaller than 50 km. However, as mentioned before, the slope discontinuity on the SSH spectrum, understandable again in terms of the IGW linear relationship between PE and KE for a given baroclinic mode, may be used to discriminate IGWs and BMs. SWOT is indeed a wide-swath satellite altimeter that will observe, both, the magnitude and the phase of the different SSH structures with scales below 100 km. This means that if IGWs in summer are dominated by a given baroclinic mode (as it seems to be from the present study), SWOT observations should allow to diagnose the KE associate with IGWs using the PE/KE relationship for this baroclinic mode (see Gill, 1982). This opens new interesting perspectives in terms of the SWOT potential.

4.3. Partition of Surface Motions Into Rotational and Divergent Components

We next analyze the BM and IGW impacts on the RV and DIV fields (Figures 10 and 11) and compare the results with those for the KE field (Figures 8). The purpose is to understand whether the partition of surface motions into rotational and divergent components allows to discriminate the respective contribution of BMs and IGWs on the KE field. Results (detailed below) emphasize an even more complex picture than the one described in section 3.2, indicating the assumption based on the DIV contribution explained only by IGWs (Böhler et al., 2014) does not hold everywhere and at any time.

On one hand, the RV field is found to be dominated by BMs in all high EKE regions of the World Ocean, both, in summer and winter (see Figures 10). Low EKE regions are also dominated by BMs in winter in both Hemispheres, but IGWs impacts in summer lead to $R \sim 1$ in these regions. On the other hand, the DIV field during summer is strongly dominated by IGWs ($R \ll 1$) in the entire 4- to 100-km wave band in the Northern Hemisphere. On the contrary, the DIV field in the Southern Hemisphere during summer is almost dominated by BMs in high EKE regions and in the South Pacific region (a low EKE region). Only in the South Atlantic region (the other low EKE region in the Southern Hemisphere) the DIV field is dominated by IGWs over the entire 4- to 100-km wave band. Thus, except for the Gulf Stream region, all other regions during summer differ from the Kuroshio-Extension region. In winter, the DIV field is dominated by BMs ($R > 1$) in all high EKE regions. In low EKE regions (except for the North-East Pacific region) the DIV field is still dominated by BMs during winter, but only in the 10–50 km.

Let us examine in more details what happens, first, in summer. On one hand, the RV field in high EKE regions of the Northern Hemisphere (Figures 10c and 10d) is almost dominated by BMs over the entire 10- to 100-km band, but in low EKE regions, BMs and IGWs impacts on the RV field are almost equally partitioned. On the other hand, the DIV field is entirely dominated by IGWs in all regions (high and low EKE regions) of this hemisphere. Referring to the KE field (Figures 8c and 8d and table), high EKE regions of this hemisphere are slightly more dominated by BMs than IGWs in the 50- to 100-km band and more dominated by IGWs in the 10–50 km. This leads to a dominance of the RV contribution (i.e., BMs) in the 50- to 100-km band and of the DIV contribution (i.e. IGWs) in the 10- to 50-km band. Thus, results for the Gulf Stream are similar to those for the Kuroshio-Extension. In low EKE regions of the Northern Hemisphere, during summer, the KE field is strongly dominated by IGWs in both wave bands. This means that (from results for the RV and DIV fields, Figures 10, and 11c and 11d) KE in these regions is mostly captured by the DIV contribution for the two scale bands in summer (since RV is dominated by BMs, Figures 10c and 10d). These results indicate that the Bühler's assumption (that assumes the DIV field dominated by IGWs) should allow to partition motions into IGWs and BMs in the Northern Hemisphere in summer.

Although the situation for the RV field during summer is almost similar in both Hemispheres (BMs dominance), the DIV field, as the KE field, differs in the Southern Hemisphere. The DIV field in all regions of this hemisphere during this season is dominated by BMs except for the South Atlantic region. This means that the Bühler's assumption should not work in this hemisphere except again for the South Atlantic region. Comparison of Figures 8c and 8d with Figures 11c and 11d indicates, however, that the DIV contribution to KE should be quite weak relatively to the RV contribution. The lack of summer enhancement of DIV due to IGWs south of 40°S is linked to the deep mixed layer. Even in summertime the mixed layer remains deep leading, on one hand, to an unfruitful trapping of IGWs and, on the other hand, to the production of SBMs through mixed layer instabilities (Qiu et al., 2018).

During winter, in both hemispheres, the RV field is dominated by BMs. The DIV fields during this season are dominated by BMs in all high EKE regions, especially in the 4- to 50-km band. In low EKE regions of both hemispheres, the DIV fields are dominated by BMs in the 4- to 50-km band (except for the NEP region) and IGWs in the 50–100 km band. These differences between the DIV fields in the 10–50 km and 50–100 km bands can be explained on one hand by the winter mixed-layer instabilities that are quite energetic in the 10- to 50-km band (Su et al., 2018). On the other hand, a ω - k spectrum (not shown) of the DIV field clearly indicates that the larger IGWs dominance in the 50- to 100-km band is explained by the contribution of internal tides and near-inertial waves, respectively, in the M₂ and f frequency bands. Comparison of these fields with those for KE (Figures 8) suggests that the RV contribution dominates KE during this season. However, the DIV contribution to the KE in the 10- to 50-km band indicates that assuming nondivergent BMs during winter in the world ocean is questionable. The only exception would be the NEP region.

As already mentioned, the results described in the section, using the Helmholtz decomposition, reveal a situation more complex than the one described in section 3.2 for the Kuroshio-Extension. However, they shed some light on what we can expect using different satellite observations. One example concerns the NEP region characterized by a dominance of IGWs in summer. SSH observations alone cannot help to partition motions into IGWs and BMs since a full SSH wave number spectrum (not shown) displays during this season only a plateau starting at 300 km. However, satellite observations of surface motions (assuming the spatial resolution is high enough) should allow to diagnose this partition using the Bühler methodology as

mentioned above. The analysis carried out in this section is preliminary. A more in-depth analysis should be the focus of a future study.

4.4. Impacts of BMs and IGWs on SST and SSS

As expected, SST (Figure 12) and SSS (not shown) in the 10- to 100-km band are totally dominated by BMs in the whole World Ocean during all seasons, even in the NEP region where the IGW impacts on the other fields seem the strongest. This generalizes what was found in section 3 for the Kuroshio-Extension region and the same explanation can be invoked. SST and SSS are horizontally advected by surface motions. But, as discussed in section 3, advection by IGWs leads SST (or SSS) displacements no larger than 4 km (again the smallest resolved length scale), explaining that IGW impacts do not show up in the ω - k SST and SSS spectra, except for energetic near-inertial waves and internal tides. SST displacements due to these large-scale waves are, however, not large enough to impact the R values. This is true in particular in the low EKE regions in the summer Northern Hemisphere, although KE in these regions is mostly explained by IGWs.

One important comment is that these characteristics do not hold for temperature and salinity below the surface. Indeed, the vertical velocity is no more zero below the surface and the one associated with IGWs can be large. Since the vertical gradients of temperature and salinity are not exactly zero, the vertical advection of these variables lead to a non-negligible IGW signature on these fields. This is what is observed on the ω - k spectra of temperature and salinity (not shown) at depth.

Coming back to SST and SSS, results of this section suggest that these fields can be potentially used to retrieve balanced motions using some methodologies proposed by previous studies (Isern-Fontanet et al., 2006; Lapeyre & Klein, 2006; Ponte & Klein, 2013; Wang et al., 2013), an approach that may be appropriate in presence of energetic IGWs (Ponte & Klein, 2015). This should be addressed in a future study.

5. Discussion and Summary

The existing observing systems of surface motions from space mostly involve satellite altimeters that allow to retrieve only motions with scales larger than 70–100 km. These motions include coherent internal tides and geostrophic motions (MBMs). Future satellite observing systems should observe surface motions with a much higher spatial resolution and in particular SBMs and IGWs. So partitioning the observed motions into BMs and IGWs is critical because of their different impacts on the ocean kinetic budget. These future satellite data will concern SSH (from the SWOT mission) and KE (from the WaCM, SKIM and WaveMill missions). Exploiting the synergy between all these future observations and existing ones with similar resolution (such as satellite SST images) should allow to diagnose not only the ocean KE but also the energy exchanges between scales and therefore the ocean KE budget. This includes the inverse KE cascade, critically impacted by small scales (Arbic et al., 2008; Qiu et al., 2014), the 3-D scattering of near-inertial and internal tidal motions by mesoscale eddies that feed the energy route to smaller scales (through IGWs) and therefore to dissipation and the energy exchanges between BMs and IGWs.

To further understand how to exploit this synergy and therefore to understand the partition of motions into BMs and IGWs in the different fields, KE, SSH, SST, and SSS, the present study has taken advantage of the high-resolution global ocean LLC4320 simulation to understand this partition in the spectral space ω - k . Results emphasize the wealth and diversity of this partition (through the analysis of ω - k spectra), which depends on the variable considered, the season, the hemisphere, and the regions (sorted out into low and high EKE regions). This valuable data set of a total of twelve thousand ω - k spectra is available on a website for further analyses.

The energy level at periods between 1 and 10 days in the LLC4320 simulation is still underestimated (Savage, Arbic, Alford, et al., 2017). In the context of the partition of ocean motions into BMs and IGWs, a more realistic energy level in this frequency band, which does not include IGWs, will increase the ratio BMs/IGWs toward the BMs dominance in the 10- to 50-km band.

BMs and IGWs occupy two different and well-defined regions in the ω - k space, separated by the dispersion relation curve associated with the highest baroclinic mode. Previous studies showed the same two regions in the ω - k space using high-resolution simulations forced with tides and high-frequency atmospheric forcing (Müller et al., 2015; Qiu et al., 2018; Rocha et al., 2016; Savage, Arbic, Alford, et al., 2017). In this study the spectra were multiplied by k and ω with two purposes: (1) emphasizing the submesoscale and high-

frequency motions and (2) preserving the variance in log-log scale presentation. In this way, we were able to characterize the seasonality of the BMs and IGWs in the 4- to 50-km wave band: pointed out the strong dominance of the SBMs in winter, often reaching frequencies much higher than f , and the strong dominance of the higher baroclinic normal modes for IGWs in summer.

The spectral analysis carried out in the Kuroshio-Extension highlights the wintertime contribution of RV to KE variance associated with SBMs for frequencies higher than f (USMs). Additionally, the DIV contribution to KE on USMs display variance close to the RV contribution (ratio ~1). They contribute for shallowing the spectral slope from k^{-3} to k^{-2} in the wintertime wave number spectra of kinetic energy (Figure 5). Such superinertial motions manifest the activity either by mixed layer instabilities (Fox-Kemper et al., 2008) or by frontogenesis (Hoskins, 1975). Regardless of their genesis, the submesoscale instabilities are characterized by a violent vertical pump in the upper ocean layer (McWilliams, 2016). Su et al. (2018) showed that the vertical heat fluxes estimated in the 10- to 50-km band are 3 times higher than the mesoscale counterpart. Moreover, McWilliams et al. (2009) demonstrated a significant restratification of the upper ocean through a filamentary intensification in the submesoscale range. The role of the balanced motions with frequencies higher than f in the ocean vertical pump deserve a more carefully study, since they might enhance the surface fluxes between the ocean and the atmosphere.

On the other hand, in summer the SBMs are absent but IGWs are energized leading to a slope discontinuity in the SSH wave number spectrum. Rocha, Gille, et al. (2016) demonstrated that this is due to the intensification in summer of the higher baroclinic modes because of the shallow mixed-layer. The summertime ω - k KE spectra display the intensification of discrete beams corresponding to mode-2 and mode-3. Furthermore, the Helmholtz decomposition performed in the present study reveals that IGW mostly explain the DIV contribution to KE at frequencies higher than f , rather than the SBMs reported in winter.

The loss of geostrophic balance, or the spectral slope discontinuity, at a given wave number in SSH spectra is consistent with the transition scale reported by Qiu et al. (2018). Taking advantage of this spectral slope discontinuity in SSH, it is possible to recover the imbalanced energy associated with IGW motions through the linear version of shallow water model. In the Kuroshio-Extension region, the third baroclinic mode was the best fit. As a matter of fact, Rocha, Gille, et al. (2016, supporting information) using in situ data from the World Ocean Atlas (Levitus et al., 2013) explained this dramatic amplification of mode-3 in summer as a consequence of a shallower mixed layer and larger density jump at the mixed layer base.

The Helmholtz decomposition in the ω - k space sheds light to better understand the kind of motions captured in the rotational and divergent part of the surface motions for both winter and summer. In winter, the DIV part is explained by not only IGWs but also SBMs with frequencies near or higher than f adding a caveat on the interpretation of the wave number spectra of KE. Finally, in summer, the RV part has a weak contribution of the third baroclinic mode. Furthermore, the ratio DIV over RV is greater than 1 indicating that the assumption of IGWs explaining the DIV part holds (Bühler et al., 2014; Qiu et al., 2017; Rocha, Gille, et al., 2016). So the methodology based on the so-called Helmholtz decomposition and using in addition the assumption of the DIV contribution entirely explained by IGWs (Bühler et al., 2014) may help to an accurately partition in summer motions into BMs and IGWs but only in specific regions. However, in winter, it may lead to an overestimation of IGWs RV contribution due to the assumption of nondivergent BMs, meaning that the DIV part is entirely explained by IGWs. So knowing a priori the information about the respective contribution of the DIV part associated with BMs and IGWs to KE allows to infer whether the assumption is accurate.

By analyzing the time-dependent atlas of the R value, we found two main results: (1) the significant differences between the Northern and Southern Hemispheres and (2) a strong regional heterogeneity in the partition of motions into IGWs and BMs. Broadly speaking, northern oceans are more affected by IGWs than southern oceans in the two wave bands considered in the present study. As we already pointed out in section 4.1, this behavior is explained in part by the more energetic internal tides in the Northern Hemisphere beyond the latitude 30°N (Savage, Arbic, Richman, et al., 2017) and by the more energetic near-inertial motions in the Northern Hemisphere (Chaigneau et al., 2008).

Embedded in this scenario, there is a strong heterogeneity on a regional scale in the partition of motions into BMs and IGWs. In regions with high-EKE levels, the RV and DIV fields are mostly dominated by BMs, in both wave bands (10–50 and 50–100 km), both in winter or summer. In low-EKE regions, the RV field is equally dominated by BMs and IGWs, whereas the DIV field is dominated by IGWs in both wave bands (10–50 and

50–100 km). Qiu et al. (2018) argued that such heterogeneity in the KE and SSH fields is set by the local mesoscale eddy variability and by the energy level of the unbalanced motions (near-inertial flows, internal tides, and inertia-gravity waves). In our extended work, we found that in the 50- to 100-km wave band, the near-inertial motions and the semidiurnal internal tides accounts to energize the unbalanced motion part of the RV and DV fields. And for the 10- to 50-km wave band, the SBMs activity for in high-EKE regions and the IGWs activity in low-EKE regions characterize the heterogeneity. The latter result highlights that the role of the local stratification is more important than expected.

Since the BMs and IGWs have different impact on the surface field, it is plausible to take advantages of the existing and future satellite observations to diagnose not only the BMs but also the IGWs motions. The present study provides a global reference framework to determine the kind of analysis that must be applied to infer the contribution of these two classes of motions on the kinetic energy budget, as a function of the dataset, the region and the season selected.

With the future SWOT-measured SSH we will have access to upper band of sub-mesoscale motions (i.e. ~10–50 km), either SBMs or IGWs. In winter, SWOT might be able to capture the SBMs in a significant part of the world ocean. In summer season, based on the spectral slope discontinuity in SSH we may have access to the IGWs kinetic energy. Since there is no spectral discontinuity in KE spectra, SWOT emerges as an invaluable instrument to diagnose BMs and IGWs observables on the tapestry of SSH.

Nevertheless, since surface motions are the result of the superposition of many oceanic processes (wind-driven currents, tides, fronts and filaments) and most of them are not in geostrophic balance, the satellite missions aimed for measuring the total surface current (WaCM, SKIM) works as a complement for SWOT. As we pointed out in the Helmholtz decomposition analysis, the DIV component contributes at the same scales as the RV component; noticing that at large wave number and at near-inertial frequencies, the DIV contributes equally or greater than RV. However, these missions have to deal with precision issues of the instruments (WaCM, Rodriguez et al., 2018, and SKIM, Arduin et al., 2018). It has to be established whether the magnitude of the divergent motions reach the requirements of the accuracy of the instrumentation.

Regarding the global SST fields, the negligible IGW impact is not surprising. Previous studies have demonstrated the potential of SST to reconstruct the 3-D dynamics under the quasi-geostrophic (Ponte et al., 2017; Ponte & Klein, 2013) and surface quasi-geostrophic (Wang et al., 2013) frameworks. Despite those studies were carried out in regions resembling high-EKE regions, the global maps of the value R showed that it is possible to recover BMs even in the low-EKE regions, that is, NEP and SA. As long as the SST retrievals are cloud-free, BMs should be recovered via potential vorticity inversion (Ponte et al., 2017).

Unfortunately, SBMs with frequencies higher than f (USMs), highly divergent, will not be measured neither by SWOT nor by WaCM nor SKIM. Here is where high-frequency radar observing system or high-resolution global ocean simulations play a critical role to better understand the rapid evolving SBMs. High-frequency radars are restricted to measure surface motions no longer than 300-km offshore (Kim et al., 2011). However, high-resolution global ocean simulations forced with high-frequency atmospheric boundary conditions and tides are a powerful tool to reveal the impact of rapid evolving SBMs and USMs in the ocean. As far as we know, the LLC4320 simulation is the state of the art in ocean numerical modeling. In the years to come, such numerical simulations will be at the forefront supporting the disentanglement of submesoscale balanced motions from internal gravity waves and contributing for facing the challenge to better understand their respective contributions on the ocean kinetic budget on a global scale.

Acknowledgments

This work was performed at the Jet Propulsion Laboratory, California Institute of Technology, under contract with the National Aeronautics and Space Administration (NASA). H. T. and D. M. were supported by NASA Physical Oceanography (PO) and Modeling, Analysis, and Prediction (MAP) Programs. P. K. was supported by a NASA Senior Fellowship, by CNES (OSTST-OSIW grant), and by the Laboratoire d'Excellence LabexMER (ANR-10-LABX-19). J. W., L. F., B. Q., and S. C. acknowledge support from the NASA SWOT mission (NNX16AH66G). Z. S. was supported by the NASA Postdoctoral Program (NPP) and by NASA grant NNX15AG42G. High-end computing resources were provided by the NASA Advanced Supercomputing (NAS) Division at the Ames Research Center. We are particularly grateful to C. Henze, B. Nelson, and D. Ellsworth for development of interactive visualization tools that helped us to explore the LLC4320 simulation. Instructions for obtaining LLC4320 model output are here: http://ecc2.org/lc_hires. The authors thank the two reviewers for their insightful comments.

References

- Alford, M. H., MacKinnon, J. A., Simmons, H. L., & Nash, J. D. (2016). Near-inertial internal gravity waves in the ocean. *Annual Review of Marine Science*, 8(1), 95–123. <https://doi.org/10.1146/annurev-marine-010814-015746>
- Arbic, B. K., Mitrovica, J. X., MacAyeal, D. R., & Milne, G. A. (2008). On the factors behind large Labrador Sea tides during the last glacial cycle and the potential implications for Heinrich events. *Paleoceanography*, 23, PA3211. <https://doi.org/10.1029/2007PA001573>
- Ardhuin, F., Aksенov, Y., Benetazzo, A., Bertino, L., Brandt, P., Caubet, E., et al. (2018). Measuring currents, ice drift, and waves from space: The sea surface kinematics multiscale monitoring (SKIM) concept. *Ocean Science*, 14(3), 337–354. <https://doi.org/10.5194/os-14-337-2018>
- Bühler, O., Callies, J., & Ferrari, R. (2014). Wave-vortex decomposition of one-dimensional ship-track data. *Journal of Fluid Mechanics*, 756, 1007–1026. <https://doi.org/10.1017/jfm.2014.488>
- Callies, J., Ferrari, R., Klymak, J. M., & Gula, J. (2015). Seasonality in submesoscale turbulence. *Nature Communications*, 6, 6861, doi:<https://doi.org/10.1038/ncomms7862>, 1, 6862.

- Capet, X., Roullet, G., Klein, P., & Maze, G. (2016). Intensification of upper-ocean submesoscale turbulence through Charney baroclinic instability. *Journal of Physical Oceanography*, 46(11), 3365–3384. <https://doi.org/10.1175/JPO-D-16-0050.1>
- Chaigneau, A., Pizarro, O., & Rojas, W. (2008). Global climatology of near-inertial current characteristics from Lagrangian observations. *Geophysical Research Letters*, 35, L13603. <https://doi.org/10.1029/2008GL034060>
- Chelton, D. B., Schlaik, M., & Samelson, R. (2011). Global observations of nonlinear mesoscale eddies. *Progress in Oceanography*, 91(2), 167–216. <https://doi.org/10.1016/j.pocean.2011.01.002>
- Ferrari, R., & Wunsch, C. (2009). Ocean circulation kinetic energy: Reservoirs, sources, and sinks. *Annual Review of Fluid Mechanics*, 41(1), 253–282. <https://doi.org/10.1146/annurev.fluid.40.111406.102139>
- Forget, G., Campin, J.-M., Heimbach, P., Hill, C. N., Ponte, R. M., & Wunsch, C. (2015). ECCO version 4: An integrated framework for non-linear inverse modeling and global ocean state estimation. *Geoscientific Model Development*, 8(10), 3071–3104. <https://doi.org/10.5194/gmd-83071-2015>
- Fox-Kemper, B., Ferrari, R., & Hallberg, R. (2008). Parameterization of mixed layer eddies. Part I: Theory and diagnosis. *Journal of Physical Oceanography*, 38(6), 1145–1165. <https://doi.org/10.1175/2007JPO3792.1>
- Fu, L.-L., & Ferrari, R. (2008). Observing oceanic submesoscale processes from space. *EOS, Transactions of the American Geophysical Union*, 89(48), 488. <https://doi.org/10.1029/2008EO480003>
- Gill, A. E. (1982). *Atmospheric-ocean dynamics*, (p. 662). New York: Academic Press.
- Hill, C., Menemenlis, D., Ciotti, B., & Henze, C. (2007). Investigating solution convergence in a global ocean model using 2048-processor cluster of distributed shared memory machines. *Scientific Programming*, 12, 107–115.
- Hoskins, B. J. (1975). The geostrophic momentum approximation and the semigeostrophic equations. *Journal of the Atmospheric Sciences*, 32(2), 233–242. [https://doi.org/10.1175/1520-0469\(1975\)032<0233:TGMAT>2.0.CO;2](https://doi.org/10.1175/1520-0469(1975)032<0233:TGMAT>2.0.CO;2)
- Isern-Fontanet, J., Chapron, B., Lapeyre, G., & Klein, P. (2006). Potential use of microwave sea surface temperatures for the estimation of ocean currents. *Geophysical Research Letters*, 33, L24608. <https://doi.org/10.1029/2006GL027801>
- Kelly, M., & Wyngaard, J. C. (2006). Two-dimensional spectra in the atmospheric boundary layer. *Journal of the Atmospheric Sciences*, 63(11), 3066–3070. <https://doi.org/10.1175/JAS3769.1>
- Kim, S. Y., Terrill, E. J., Cornuelle, B. D., Jones, B., Washburn, L., Moline, M. A., Paduan, J. D., et al. (2011). Mapping the U. S. West Coast surface circulation: A multiyear analysis of high-frequency radar observations. *Journal of Geophysical Research*, 116, C03011. <https://doi.org/10.1029/2010JC006669>
- Klein, P., & Lapeyre, G. (2009). The oceanic vertical pump induced by mesoscale and submesoscale turbulence. *Annual Review of Marine Science*, 1(1), 351–375. <https://doi.org/10.1146/annurev.marine.010908.163704>
- Lapeyre, G., & Klein, P. (2006). Dynamics of the upper oceanic layers in terms of surface quasigeostrophy theory. *Journal of Physical Oceanography*, 36(2), 165–176. <https://doi.org/10.1175/JPO2840.1>
- Levitus, S., Antonov, J. I., Baranova, O. K., Boyer, T. P., Coleman, C. L., Garcia, H. E., et al. (2013). The world ocean database. *Data Science Journal*, 12, WD,S229–WD,S234.
- Losch, M., Menemenlis, D., Heimbach, P., Campin, J.-M., & Hill, C. (2010). On the formulation of sea-ice models. Part 1: Effects of different solver implementations and parameterizations. *Ocean Modelling*, 33(1-2), 129–144. <https://doi.org/10.1016/j.ocemod.2009.12.008>
- Lumpkin, R., Grodsky, S., Centurioni, L., Rio, M.-H., & Carton, J. (2012). Removing spurious low-frequency variability in drifter velocities. *Journal of Atmospheric and Oceanic Technology*, 30(2), 353–360. <https://doi.org/10.1175/JTECH-D-12-00139.1>
- Marshall, J. A., Adcroft, A., Hill, C., Perelman, L., & Heissey, C. (1997). A finite volume, incompressible Navier-Stokes model for studies of the ocean on parallel computers. *Journal of Geophysical Research*, 102, 5753–5766. <https://doi.org/10.1029/96JC02775>
- Martin, A. C. H., Gommenginger, C., Marquez, J., Doody, S., Navarro, V., & Buck, C. (2016). Wind-wave-induced velocity in ATI SAR ocean surface currents: First experimental evidence from airborne campaign. *Journal of Geophysical Research: Oceans*, 121, 1640–1653. <https://doi.org/10.1002/2015JC011459>
- McWilliams, J. C. (2016). Submesoscale currents in the ocean. *Proceedings of the Royal Society A*, 472(2189). <https://doi.org/10.1098/rspa.2016.0117>
- McWilliams, J. C., Colas, F., & Molemaker, M. J. (2009). Cold filamentary intensification and oceanic surface convergence. *Geophysical Research Letters*, 36, L18602. <https://doi.org/10.1029/2009GL039402>
- Menemenlis, D., Campin, J.-M., Heimbach, P., Hill, C., Lee, T., Nguyen, A., et al. (2008). ECCO2: High resolution global ocean and sea ice data synthesis. *Mercator Ocean Quarterly Newsletter*, 31, 13–21.
- Mensa, J. A., Garrafo, Z., Griffa, A., Özgökmen, T. M., Haza, A., & Veneziani, M. (2013). Seasonality of the submesoscale dynamics in the Gulf Stream region. *Ocean Dynamics*, 63, 923–941. <https://doi.org/10.1007/s10203-013-0633-1>
- Müller, M., Arbic, B. K., Richman, J. G., Shriver, J. F., Scott, R. B., Wallcraft, A. J., & Zamudio, L. (2015). Toward and internal gravity waves spectrum in a global ocean models. *Geophysical Research Letters*, 42, 3474–3481. <https://doi.org/10.1002/2015GL063365>
- Polzin, K. L., & Lvov, Y. L. (2011). Toward a regional characterization of the oceanics internal wavefield. *Reviews of Geophysics*, 49, RG4003. <https://doi.org/10.1029/2010RG000329>
- Ponte, A. L., & Klein, P. (2013). Reconstruction of the upper ocean 3D dynamics from high resolution sea surface height. *Ocean Dynamics*, 63(7), 777–791. <https://doi.org/10.1007/s10236-013-0611-7>
- Ponte, A. L., & Klein, P. (2015). Incoherent signature of internal tides observed on sea level in idealized numerical simulations. *Geophysical Research Letters*, 42, 1520–1526. <https://doi.org/10.1002/2014GL062583>
- Ponte, A. L., Klein, P., Dunphy, M., & Le Gentil, S. (2017). Low-mode internal tides and balanced dynamics disentanglement in altimetric observations: Synergy with surface density observations. *Journal of Geophysical Research: Oceans*, 122, 2143–2155. <https://doi.org/10.1002/2016JC012214>
- Qiu, B., Chen, S., Klein, P., Sasaki, H., & Sasai, Y. (2014). Seasonal mesoscale and submesoscale eddy variability along the North Pacific Subtropical Concurrent. *Journal of Physical Oceanography*, 44(12), 3079–3098. <https://doi.org/10.1175/JPO-D-14-0071.1>
- Qiu, B., Chen, S., Klein, P., Wang, J., Torres, H., Fu, L.-L., & Menemenlis, D. (2018). Seasonality in transition scale from balanced to unbalanced motions in the world ocean. *Journal of Physical Oceanography*, 48(3), 591–605. <https://doi.org/10.1175/JPO-D-17-0169.1>
- Qiu, B., Nakano, T., Chen, S., & Klein, P. (2017). Submesoscale transition from geostrophic flows to internal waves in the northwestern Pacific upper ocean. *Nature Communications*, 8, 14055. <https://doi.org/10.1038/ncomms14055>
- Richman, J. G., Arbic, B. K., Shriver, J. F., Metzger, E. J., & Wallcraft, A. J. (2012). Inferring dynamics from wavenumber spectra of an eddying global ocean model with embedded tides. *Journal of Geophysical Research*, 117, C12012. <https://doi.org/10.1029/2012JC008364>
- Rocha, C. B., Chereskin, T. K., Gille, S. T., & Menemenlis, D. (2016). Mesoscale to submesoscale wavenumber spectra in Drake Passage. *Journal of Physical Oceanography*, 46(2), 601–620. <https://doi.org/10.1175/JPO-D-15-0087.1>
- Rocha, C. B., Gille, S. T., Chereskin, T. K., & Menemenlis, D. (2016). Seasonality of submesoscale dynamics in the Kuroshio Extension. *Geophysical Research Letters*, 43, 11,304–11,311. <https://doi.org/10.1002/2016GL071349>

- Rodriguez, E., Wineteer, A., Perkovic-Martin, D., Gal, T., Stiles, B. W., Niamsuwan, N., & Rodriguez Monje, R. (2018). Estimating ocean vector winds and currents using a Ka-band pencil-beam Doppler scatterometer. *Remote Sensing*, 10(4), 576. <https://doi.org/10.3390/rs10040576>
- Rosso, I., McC, A., Hogg, A. E., Kiss, R., Matear, A. K., & van Sebille, E. (2014). Vertical transport in the ocean due to sub-mesoscale structures: Impacts in the Kerguelen region. *Ocean Modelling*, 80, 10–23. <https://doi.org/10.1016/j.ocemod.2014.05.001>
- Sasaki, H., Klein, P., Qiu, B., & Sasai, Y. (2014). Impact of oceanic-scale interactions on the seasonal modulation of ocean dynamics by the atmosphere. *Nature Communications*, 5(1), 5636. <https://doi.org/10.1038/ncomms6636>
- Savage, A. C., Arbic, B. K., Alford, M. H., Ansong, J. K., Farrar, J. T., Menemenlis, D., et al. (2017). Spectral decomposition of internal gravity waves sea surface height in global maps. *Journal of Geophysical Research: Oceans*, 122, 7803–7821. <https://doi.org/10.1002/2017JC013009>
- Savage, A. C., Arbic, B. K., Richman, J. G., Shriner, J. F., Alford, M. H., Buijsman, M. C., et al. (2017). Frequency content of sea surface height variability from internal gravity waves to mesoscale eddies. *Journal of Geophysical Research: Oceans*, 122, 2519–2538. <https://doi.org/10.1002/2016JC012331>
- Su, Z., Wang, J., Klein, P., Thompson, A., & Menemenlis, D. (2018). Ocean submesoscales as key component of the global heat budget. *Nature Communications*, 9(1), 775. <https://doi.org/10.1038/s41467-018-02983-w>
- Vallis, G. K. (2006). *Atmospheric and oceanic fluid dynamics*. Cambridge, England: Cambridge University Press. <https://doi.org/10.1017/CBO9780511790447>
- Wang, J., Flierl, G. R., LaCasce, J. H., McClean, J. L., & Mahadavan, A. (2013). Reconstructing the ocean's interior from surface data. *Journal of Physical Oceanography*, 43(8), 1611–1626. <https://doi.org/10.1175/JPO-D-12-0204.1>
- Wang, J., Fu, L.-L., Qiu, B., Menemenlis, D., Farrar, J. T., Chao, Y., et al. (2018). An observing system simulation experiment for the calibration and validation of the surface water and ocean topography sea surface height measurement using in-situ platforms. *Journal of Atmospheric and Oceanic Technology*, 35(2), 281–297. <https://doi.org/10.1175/JTECH-D-17-0076.1>
- Xu, Y., & Fu, L.-L. (2012). The effects of altimeter instrument noise on the estimation of the wavenumber spectrum of sea surface height. *Journal of Physical Oceanography*, 42(12), 2229–2233. <https://doi.org/10.1175/JPO-D-12-0106.1>
- Zaron, E. D. (2015). Non-stationary internal tides observed using dual-satellite altimetry. *Journal of Physical Oceanography*, 45(9), 2239–2246. <https://doi.org/10.1175/JPO-D-15-0020.1>